2017

Development of the Focal Plane Instrumentation of the SEparator for CApture Reactions (SECAR)

Kyle Joerres
Louisiana State University and Agricultural and Mechanical College, kyle.joerres@snc.edu

DEVELOPMENT OF THE FOCAL PLANE INSTRUMENTATION OF THE SEPARATOR FOR CAPTURE REACTIONS (SECAR)

A Thesis

Submitted to the Graduate Faculty of the
Louisiana State University and
Agricultural and Mechanical College
in partial fulfillment of the
requirements for the degree of
Master of Science

in

The Department of Physics and Astronomy

by
Kyle Christopher Joerres
B.S., St. Norbert College, 2015
May 2017

To my father,

Mark Joerres,

For always showing me the value of hard work.

ACKNOWLEDGMENTS

A lot of people helped me get to where I am and their guidance and support is immeasurable. First, I'd like to thank my parents, family, and friends for their constant love and guiding support. To my fiancé, Titi, I'd like to say a special thank you for all the encouragement and confidence given ever since we met. I'd like to thank those that helped me through my time at LSU and especially with the writing of this thesis. I'd like to especially thank Dr. Jeffery Blackmon for the constant direction and improvement with this thesis. I'd also like to thank those that helped me through my time at LSU, as well as with this thesis, such as Dr. Scott Marley, Dr. Catherine Deibel and my office mates Alex Laminack, Ashley Hood and Erin Good. I'd also like to thank the members of the SECAR collaboration, especially Michael Larmann and Aftab Hussain. This work is supported by the U.S. Department of Energy Office of Science, Office of Nuclear Physics under Award Number DE-FG02-96ER40978 and by Award Number DE-SC0014384.

TABLE OF CONTENTS

LIST OF TABLES

LIST OF FIGURES

ABSTRACT

The SEparator for CApture Reactions (SECAR) is currently being developed at the National Superconducting Cyclotron Laboratory (NSCL) and the future Facility for Rare Isotope Beams (FRIB) for measurements of nuclear reactions critical for understanding energy generation and element synthesis in stellar explosions. SECAR is an electromagnetic recoil separator designed for sensitive measurements of radiative capture reactions using beams of proton-rich, short-lived isotopes at the energies relevant for explosive environments such as Type I X-ray bursts and classical novae. SECAR is designed to efficiently separate capture reaction products of interest from the incident beam by up to a factor of 10^{17} by use of the separator and detection systems together.

This thesis focuses on the initial design of the focal plane for SECAR, including a preliminary suite of detectors and the supporting infrastructure. The recoils from capture reactions that reach SECAR's focal plane can be discriminated from scattered beam by velocity (via time-of-flight), trajectory, total energy, and relative energy-loss measurements. The initial instruments include a pair of transmission detectors based on metal-foil, micro-channel plates that are separated by a drift length to provide an accurate time-of-flight measurement and discriminate recoils from the generally higher velocity scattered beam. The recoils are ultimately stopped, and their full energy measured, in either a silicon (Si) strip detector or gas-filled ionization chamber. At higher energies, the gas-filled ionization chamber provides selective determination of the atomic number via a relative energy-loss measurement. An ionization chamber for implementation into the SECAR focal plane that augments the traditional relative energy-loss measurement with a position-sensitive capability has been designed and constructed. The effectiveness of the different techniques varies; at lower energies (below about 0.5 MeV/A) relative energy loss becomes less effective and a full energy measurement with a silicon strip detector provides better resolution. A flexible

infrastructure was designed using the CAD software Autodesk Inventor to allow the focal plane configuration to be optimized for the best performance for each experiment given the wide range of beam conditions expected in the scientific program that is envisioned with SECAR.

CHAPTER 1. INTRODUCTION

The SEparator for CApture Reactions (SECAR) will be an experimental end station at the ReA3 reaccelerated beam facility at the National Superconducting Cyclotron Laboratory (NSCL) and the Facility for Rare Isotope Beams (FRIB) at Michigan State University. FRIB, which will be operational by 2022, will be a leading facility in the world for nuclear science using short-lived nuclei.

The design of SECAR is optimized for measurements of low-energy capture reactions vital to understanding energy generation and element synthesis in classical nova explosions, X-ray bursts, and other stellar explosions. The layout of SECAR is shown in Fig. 1-1. A beam of unstable nuclei is accelerated by the ReA3 linear accelerator to typical energies from several hundred keV/A up to 3 MeV/A and bombards the Jet Experiments in Nuclear Structure and Astrophysics (JENSA), which is a windowless gas jet target system [1,2]. Thus, direct measurements are performed in inverse kinematics since the reactions of interest involve the capture of a target of protons or alpha particles by a beam of much heavier proton-rich nuclei that are too short-lived to be made into a target.

The capture reaction cross sections of interest are very small, resulting in low yields, and creating a single fusion product for typically 10^{11}-10^{15} unreacted beam particles. Further complicating matters, the unreacted beam particles have nearly the same momentum as the capture reaction products because the gamma rays emitted in the reaction carry away little momentum. However, the difference in mass between the reaction products and the unreacted beam particles implies a velocity difference that can be exploited to distinguish one from the other. A high rejection efficiency of the incident beam for the eventual detection of the recoils at the focal plane is necessary to allow a direct determination of astrophysical reaction rates through measurements of very low

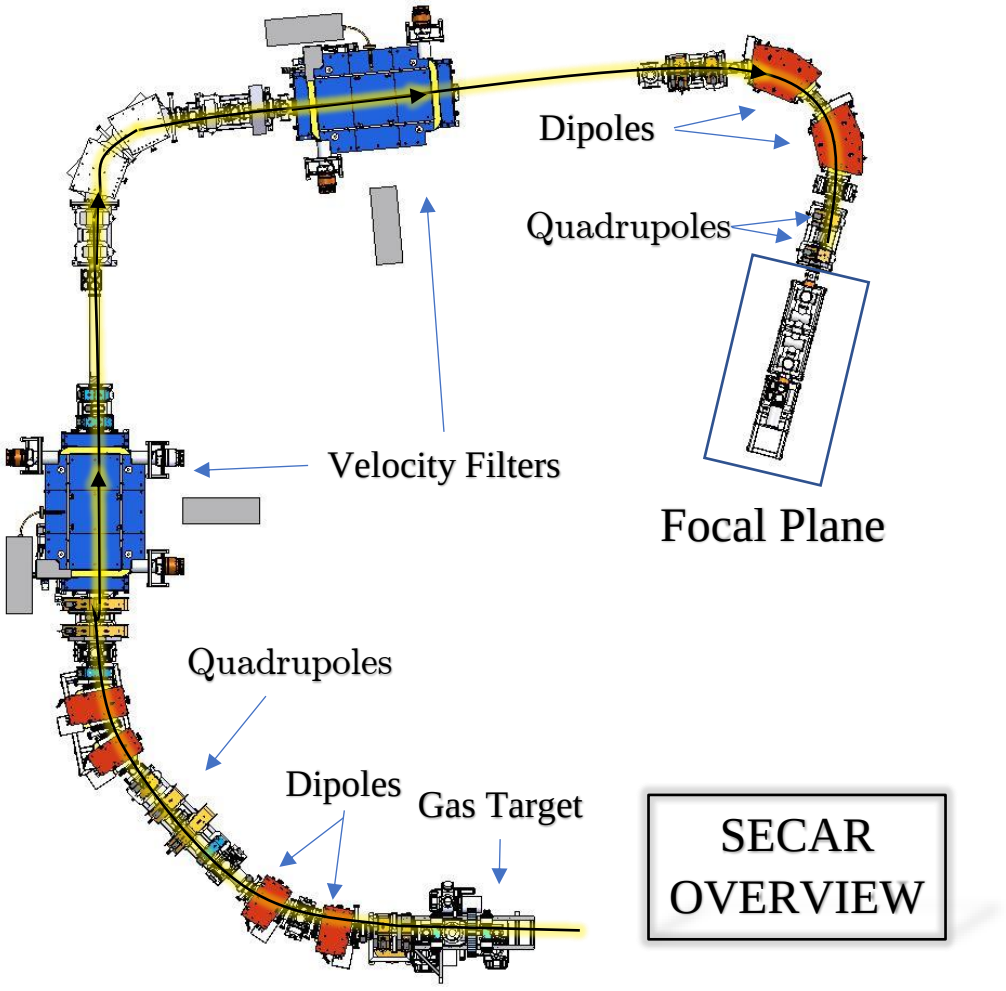

Figure 1-1: Overview of SECAR beamline from gas target to final focal plane where recoils are detected. Recoil separation accomplished with a number of components shown here with varying colors: dipole magnets (orange), Wien velocity filters (blue), and quadrupole focusing magnets (yellow).

cross sections. Physical separation of the desired recoils from the beam particles will be accomplished with both Wein velocity filters and dipole magnets for an ultimate beam rejection factor of 10^{13} at the detection system, reducing the fraction of recoils to unreacted beam particles to better than 1 in 10^{4} [2].

When the beam projectiles reach JENSA, the windowless gas target, they are in a single charge state. As they enter the target, however, interactions with the gas cause multiple charge states to be produced. Most of the projectiles exit the target without

any nuclear interaction but have a distribution of charge states dependent on the incident beam species, energy and target thickness. The first stage of the SECAR separator disperses by magnetic rigidity using dipoles to select a single charge state of the beam and recoils.

Discrimination of the beam from recoils is provided by velocity filters that have magnetic and electric fields perpendicular to each other and the ion-optical axis. Those particles with velocities (v) equal to the ratio of electric (E) to magnetic (B) fields, or $v = E/B$, pass through the filters without deflection. Velocity filters spatially separate the reaction products from the incident beam, meaning the unreacted beam can be blocked by use of appropriately placed slits. The dispersion of the magnetic dipoles and velocity filters is combined to produce a dispersion of particles at the focal plane by charge-to-mass ratio (q/A). After this electromagnetic separation, the identification of the unreacted leaky beam and reaction recoils must be carried out by the discriminating power of the detectors.

SECAR is designed for measurements using beams with masses up to $A = 65$ to match the reactions of interest in astrophysics. The center-of-mass energy of the beam can also be varied from 0.3 MeV/A to more than 3.0 MeV/A to match the most important energies in astrophysical sites such as X-ray bursts and classical novae. A wide range of beam purities may also exist for experiments depending on the required isotope and performance of the gas catcher and charge breeder [2]. These factors must be taken into account in the design and implementation of the detectors at the focal plane. The detectors will identify the desired recoils, and distinguish them from unreacted beam particles and possible reactions on beam contaminants, for a wide variety of experimental parameters.

An initial suite of detectors suited for a broad range of conditions has been designed including a set of metal-foil, micro-channel plate detectors for time-of-flight and position measurements, and an ionization chamber for atomic number Z

discrimination by a relative energy-loss measurement. A silicon strip detector is also included in the initial suite of instruments, and can be used in place of the gas ionization detector. The silicon strip detector is particularly useful when the beam is relatively low-energy (less than 0.5 MeV/A), where particle identification by relative energy-loss is ineffective and the superior energy resolution of silicon for total energy measurements is preferred. The design and initial development of the focal plane layout and detector configuration for SECAR are discussed in this thesis.

The entire focal plane structure has been designed with the CAD tool Autodesk Inventor. The designs are similar to other SECAR components and chambers but are matched to the specifications of the ion-optical trajectories and needs of the detection instrumentation that the structure will house. These designs are included within this thesis to be used as a reference for further development of the SECAR focal plane. An important feature of the SECAR focal plane is its ability to be adapted and be flexible to the needs of the experiment as the beam properties and energies will be different for each experiment, and the detection capabilities should be optimized to the experimental conditions. With this in mind, the focal plane chambers and stands were designed with additional ports for diagnostic access or detector replacement, and the capability of easy substitution or addition of further detectors for future upgrades.

CHAPTER 2. MOTIVATION

2.1. Astrophysical Impact

Nuclear physics plays a pivotal role in understanding how astrophysical phenomena behave. The modeling of astrophysical sites requires accurate nuclear reaction rates. Simulations of stellar explosions such as X-ray bursts, supernovae, and classical novae require reaction rates on unstable exotic nuclei to correctly model the nucleosynthesis and explosion processes. In classical novae, for example, observations of elemental abundances in their thermonuclear explosion ejecta give information on the synthesis of radioactive isotopes. Short-lived isotopes, such as ^{14}O, ^{15}O, and ^{17}F that reach the outer accretion envelope have β-decays that provide an important energy source for the ejection of material [3].

In both classical novae and X-ray bursts, the extreme temperatures of 10^8-10^9 K and densities of 10^4-10^6 g/cm^3 result in a sequence of reactions on unstable, proton-rich nuclei that drive the thermonuclear runaway, influencing nucleosynthesis and the rate of energy production [4,5]. Such reactions can play an important role in the nucleosynthesis and energy generation occurring in other types of stellar explosions [6,7]. Sensitivity studies using computational models have identified certain reaction rates that have a significant impact on astronomical observables such as the light curves, expansion timescales, and ejecta composition for novae [3]. Uncertainties in the rates of nuclear reactions hamper the accuracy of nucleosynthesis models and, consequently, the understanding of the observables of such astrophysical events [8,9]. In most cases, the ability to measure these important reaction rates directly is limited by the intensity of the radioactive ion beam needed to measure the reaction.

Novae and X-ray bursts are reoccurring phenomena at a stellar site with possible reoccurrence times on the order of more than 10^4 years for novae, to as short as hours for X-ray bursts [8]. The astrophysical objects that remain after stellar explosions, such as a white dwarf after novae or a neutron star after X-ray bursts, are affected by the

elements produced in the nuclear explosions. The ash composition is important for understanding phenomena such as "superbursts" and the possible link between novae and Type Ia supernova progenitors [10]. For models that track nucleosynthesis, uncertainty in the reaction rates produce uncertainties in the final elemental abundances. These uncertainties propagate further since the ashes in previous explosions impact reactions in successive explosions. Properties such as the crust structure, temperature, and composition of a neutron star are affected by the ashes of the explosion, which can be used to constrain the reaction sequences over time that convert the proton-rich ashes into extremely neutron-rich nuclei [8,10,11].

Thermonuclear reaction rates are thermal averages of an energy-dependent reaction cross section over a range of energies at a given stellar temperature, T, given by:

$$\langle \sigma v \rangle = \left(\frac{8}{\pi\mu}\right)^{1/2} \left(\frac{1}{kT}\right)^{3/2} \int_0^\infty \sigma(E)\, E\, exp\left[-\frac{E}{kT}\right] dE \qquad (1)$$

where $\langle \sigma v \rangle$ is the reaction rate, μ is the reduced mass of the particles, E is the energy, $\sigma(E)$ is the cross section of the reaction at a given energy, and k is the Boltzmann constant [12]. The reaction rates are crucial input for simulations of the detailed physics of extreme stellar environments. Understanding these reactions in novae and X-ray bursts can also be used to understand the nuclear processes, like nucleosynthesis, occurring in other stellar explosions. Population III stars are another example of an astrophysical site where the energy release and explosion mechanisms are highly dependent on reaction rates, and for a simulation to reliably predict their evolution, highly accurate reaction rates must be known [13]. Knowing important details like reaction rates gives information that connects subatomic physics at the nuclear scale to astrophysics at the Galactic scale.

Novae occur in a binary star system when material from a companion star overflows its Roche lobe and accretes onto the surface of a white dwarf. As the material

is accreted, its gravitational energy releases causing it to compress and heat while its temperature and density increase to values of 10^8 K and 10^4 g/cm^3 respectively, with novae on carbon-oxygen (CO) white dwarfs achieving lower peak temperatures than those occurring on oxygen-neon (ONe) white dwarfs [2,3,14]. Nuclear burning increases the temperature and rates of reactions, leading to thermonuclear runaway. The explosions themselves occur on the surface layer of the white dwarf and are fueled by hydrogen and helium from the envelope of the companion star. This environment is responsible for the synthesis of light- and intermediate-mass elements (up to A ~ 40 in the case of ONe novae) through radiative proton captures on unstable nuclei, though energy production in most novae is dominated by the CNO cycles [14,15]. During these bursts, energy is carried away by photons in the capture reactions as well as the ejection of mass from the thermonuclear runaway explosion.

The luminosity of a nova reaches typical maximum values of 10^4-10^5 $L_\odot$, increasing its pre-nova luminosities by a factor of 10^6 in timescales of less than a minute [14]. The luminosity then decreases to its pre-nova level over the course of several days to several months, depending on its classification [2]. The collection of spectra and the light curves over this time give information about the properties and composition of the expanding nova envelope [14]. The material that is ejected during a nova can also be determined by the absorption lines in the spectrum. These inferred elemental abundances provide a record of the thermonuclear runaway, its peak temperatures, and expansion timescales of the nova [14]. Classical novae are noteworthy contributors to a few rare isotopes in the Galaxy, like ^{13}C, ^{15}N, and ^{17}O, which are difficult to produce in any other stellar environment [16]. Also, the abundance of carbon, nitrogen and oxygen in the ejecta further supports that mixing takes place of the accreted material with the material from the CO or ONe white dwarf layers; however, this mechanism for mixing is an unanswered question in nova studies and requires a better understanding of reaction rates to improve models and their comparison with observables [14].

Questions pertaining to the thermonuclear energy generation and nucleosynthesis in novae require rates of proton capture reactions on proton-rich unstable nuclei that occur during the explosion. Some of the most significant capture reactions in novae involve the lighter nuclei closer to stability where the beam intensities at the ReA3 facility at the NSCL will be largest. One such important reaction is ^{30}P(p,γ) which is critical for the production of elements between mass 30 and 40 in novae. The reaction rate of ^{30}P(p,γ) also determines the Si isotopic ratios that have been observed in presolar meteorite grains with a nova origin, which gives clues to their stellar sources and overall contribution to Galactic abundances [3]. There are many other important reactions for novae including ^{22}Na(p,γ), which produces radioactive ^{22}Na that is a target for astronomical γ-ray observatories.

Similar to novae, X-ray bursts result from thermonuclear runaway caused by the accretion of a hydrogen- or helium- rich envelope from a companion star onto the surface of a neutron star [5]. Thermonuclear runaway is powered by the capture of protons and alpha particles on proton-rich unstable nuclei. This thermonuclear process happens within seconds, reaching maximum temperatures around 10^9 K and releasing an enormous amount of energy of roughly 10^{41} ergs primarily in the form of X-rays. The burst ends when the local hydrogen is depleted or when the envelope expands and cools enough to inhibit thermonuclear reactions [2].

Notably, the temperatures reached during X-ray bursts are higher than that of novae. Nuclear fusion through the hot CNO cycle increases the temperature until triple-alpha burning ignites to form ^{12}C. The CNO cycle breaks out into the production of heavier elements through a sequence of (α,p) and (p,γ) reactions known as the αp-process. The αp-process, which is responsible for the rise of the burst light curve, ceases around mass 20-40 depending on the temperature, which even in the hottest bursts,

ends in the Scandium ($Z = 21$) region due to the increasing Coulomb barrier for alpha-induced reactions [8].

Heavier nuclei past this point are formed via the rp-process, a sequence of rapid proton captures with time scales typically less than that of subsequent beta decay, causing the unstable nuclei to increase in mass number along the proton drip line. Despite being a much faster hydrogen-burning mechanism compared to the CNO cycle, the rp-process is a slower burning process compared to helium burning, due to some slow β-decays that occur along its path [8]. This produces a relatively slow decline in the X-ray flux. Depending on the properties of the explosion, the rp-process produces heavier elements with the upper limit imposed by alpha-unbound nuclei, causing even the most intense environments to stop the process at ^{105}Te with the closed SnSbTe cycle [17].

The intensity of X-ray bursts increases drastically on the order of seconds and then slowly reduces over the course of tens of seconds to many hours, or even days for the classification of "superbursts" [8,10]. The bursts are also recurring, in some instances as fast as on the order of hours. X-ray bursts are the most frequent thermonuclear explosions in our Galaxy with about 100 systems known, and are observed by orbiting observatories that measure their X-ray intensity as a function of time. These light curves provide information on the nature of the thermonuclear explosions and the reactions occurring within them. After burning takes place, the ashes of the event are incorporated into the surface of the neutron star crust and therefore contribute to the evolution of the star, which influences the behavior of future bursts.

Many X-ray burst observations exist because they are the most common thermonuclear explosions in our Galaxy, yet the cause of some behaviors, such as the observed double or triple peaked bursts or superbursts, is still uncertain [8,9,17]. These questions regarding X-ray bursts, particularly the duration and periodicity of some bursts, can be better understood by comparing observations to models with improved

reaction rate accuracy. The burst properties can be used to discover the underlying properties of the binary system, like accretion rate and neutron star mass [18]. In the past decade, one-dimensional simulations of X-ray bursts have reliably reproduced recurrence times and energies that agree with observations for certain subsets of X-ray bursts. Within these simulations, the reaction path the thermonuclear runaway takes in burning can be determined, giving information on the detailed nucleosynthesis evolution including how the ash composition of one burst can affect the next [9,19]. See Fig. 2-1 for an example of the reaction path in an X-ray burst.

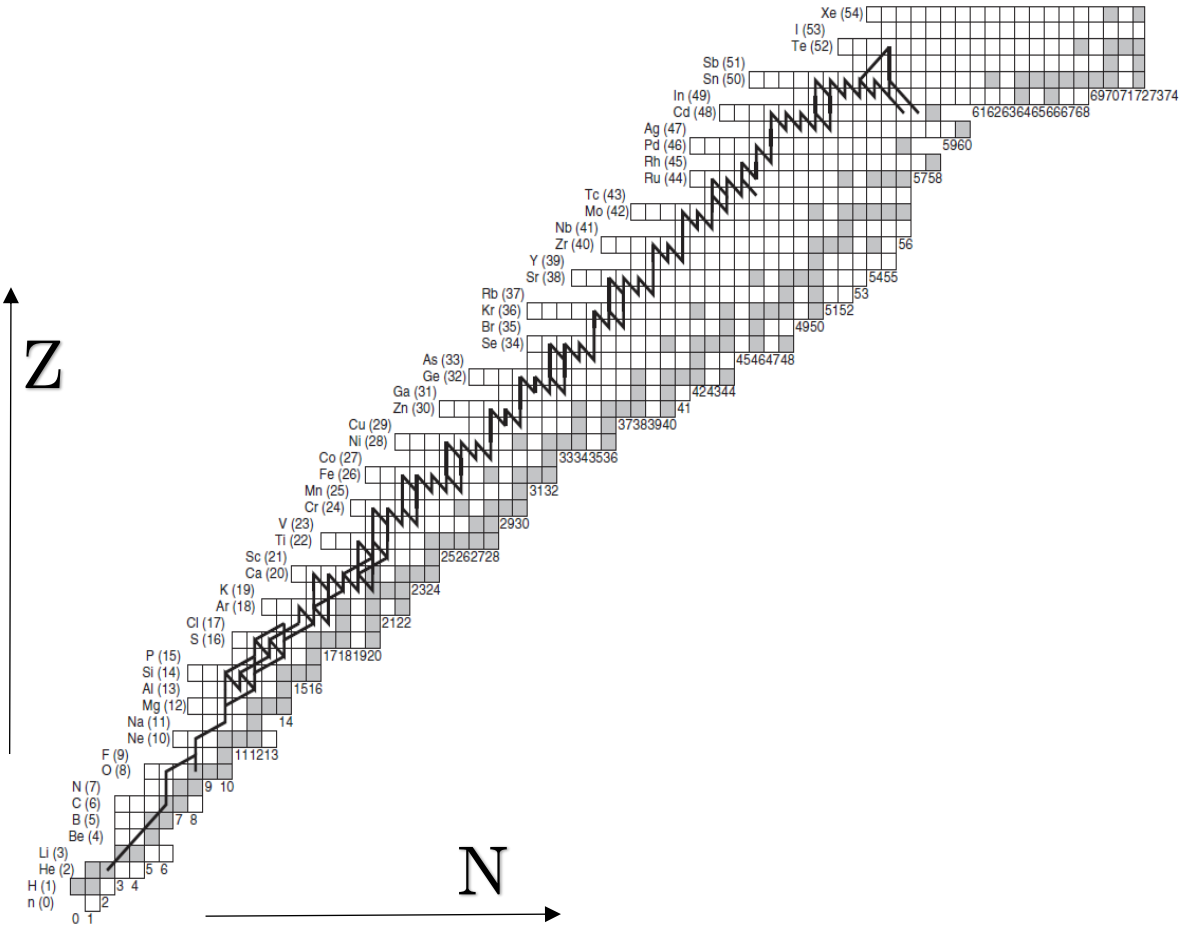

Figure 2-1: Predicted path of the rp-process in a one-zone X-ray burst model. Shaded squares denote stable nuclei [8].

A better understanding of X-ray bursts requires better knowledge of proton- and alpha-induced reaction rates on proton-rich unstable nuclei. Sensitivity studies have identified the most influential reactions affecting the light curve, the likely path nucleosynthesis takes during burning, and its subsequent possible end point [9,20]. However, significant uncertainties in reaction rates make these properties uncertain. For example, there are $N = Z$ nuclei along the proton drip line above mass 60, such as ^{64}Ge, ^{68}Se, ^{72}Kr and ^{76}Sr that impede the production of heavier elements due to their weak proton capture rate and slow beta decay that consistently appear as important in sensitivity studies. Proton-capture reactions on these so-called "waiting point" nuclei have never been directly measured, and one of the first experiments at SECAR might be ^{64}Ge(p,γ)^{65}As [2].

2.2. Contribution of SECAR

The determination of reaction rates important for stellar environments such as novae and X-ray bursts requires better low-energy measurements of capture cross sections with radioactive nuclei compared to what is presently possible due to the lack of high-intensity radioactive ion beams, and the low nuclear cross sections at the energies of interest. The cross sections generally cannot be extrapolated to lower energies, as is often done for quiescent stellar burning, as the reactions of interest for stellar explosions have resonances that dominate the reaction rate [21]. The higher intensities of radioactive ion beams at FRIB combined with the sensitivity of SECAR will allow direct measurements of reactions and weaker resonances that have not been previously accessible, but are vital to understanding astrophysical explosions such as novae and X-ray bursts. SECAR will explore reactions in the energy range of about 0.3 – 3 MeV/A, and allow for the measurement of reaction rates of (p,γ) and (α,γ) reactions of masses in the range $A = 15 - 65$.

SECAR will be housed in the experimental hall of the ReA3 facility at FRIB. The ReA3 facility is capable of accelerating ions with a charge-to-mass ratio (q/A) of 0.25 from energies of 300 keV/A to 3 MeV/A and q/A of 0.5 from energies of 300 keV/A to 6 MeV/A with a spread of only a few keV/A [2].

The intensity of the beams SECAR will use is of utmost importance due to the low cross sections at astrophysical energies that have been a major obstacle in astrophysical studies [8,21]. The beam intensities at NSCL and FRIB have been estimated, and for the initial available gas-based stopping devices, a maximum beam intensity is expected to be 10^9 particles per second (pps) (although with beams that can be extracted from solids, like oxygen, a higher intensity of the order 10^{11} pps can be achieved if a solid stopper is implemented) [2]. Such predictions are summarized in Table 2-1 and are overlaid on some reaction paths in an X-ray burst simulation in Fig. 2-2.

Table 2-1: Predicted beam intensities for important capture reactions based on ReA3 extrapolation with the NSCL driver or the FRIB driver. *The quoted intensities neglect additional losses from transport through the solid stopper for chemically reactive beams [2].

Beam	ReA3 at NSCL Projected Intensity (pps)	ReA3 at FRIB Projected Intensity (pps)*
^{15}O		$2.3 \cdot 10^{11}$
^{22}Na	$5.5 \cdot 10^{7}$	$8.3 \cdot 10^{10}$
^{23}Mg	$5.9 \cdot 10^{7}$	$3.0 \cdot 10^{10}$
^{25}Al	$1.8 \cdot 10^{6}$	$4.8 \cdot 10^{10}$
^{27}Si	$2.5 \cdot 10^{6}$	$9.6 \cdot 10^{10}$
^{29}P	$3.7 \cdot 10^{6}$	$3.4 \cdot 10^{10}$
^{30}P	$1.5 \cdot 10^{7}$	$1.4 \cdot 10^{11}$
^{33}Cl	$1.3 \cdot 10^{7}$	$2.5 \cdot 10^{10}$
^{34}Cl	$7.3 \cdot 10^{7}$	$1.1 \cdot 10^{11}$
^{35}Ar	$5.6 \cdot 10^{7}$	$5.7 \cdot 10^{10}$
^{37}K	$6.8 \cdot 10^{6}$	$1.7 \cdot 10^{10}$
^{38}K	$4.2 \cdot 10^{7}$	$8.9 \cdot 10^{10}$

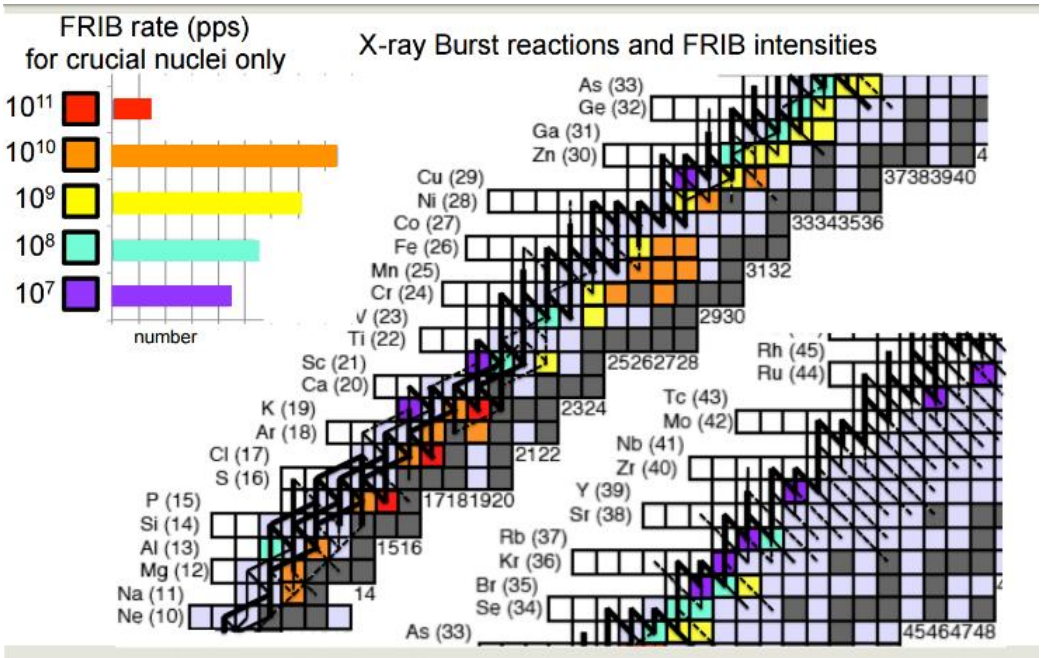

Figure 2-2: An X-ray burst reaction track overlaid with projected FRIB intensities [4].

The feasibility of obtaining sufficient statistics in a reasonable amount of beam time depends on the reaction yield, the number of reactions that occur per incident beam particle. The reaction yield determines the duration of experiments and also gives the needed rejection of the unreacted beam from the recoils that must take place for selective detection at the focal plane. The astrophysically important reactions that SECAR will measure will be primarily dominated by resonances. The yield of a narrow resonance Y_r can be approximated by [2,5]:

$$Y_r = \left[\frac{\pi^2(\hbar c)^2}{\mu c^2} E_r\right]\left[\frac{\omega\,\gamma_r}{\varepsilon_r}\right] \tag{2}$$

where E_r is the energy of the resonance, ε_r is the effective stopping power of the beam in the target in the center-of-mass system evaluated at E_r, μ is the reduced mass of the system and $\omega\gamma_r$ is the resonance strength, defined by:

$$\omega\,\gamma_r = \left[\frac{(2J_r+1)}{(2J_1+1)(2J_2+1)}\right]\frac{\Gamma_{ent}\Gamma_{exit}}{\Gamma_{tot}} \tag{3}$$

where J_r, J_1, and J_2 are the spins of the resonance and the two initial particles, respectively. Also, Γ_{ent}, Γ_{exit}, and Γ_{tot} are the widths of the entrance channel, exit channel and total width.

While this formula for resonance yields assumes a narrow resonance fully contained in the target, the assumption that the energy loss of the beam in the target is larger than the energy width of the resonance is true for nearly all the resonances that will be studied in SECAR [2]. The resonance yield depends linearly on the resonance strength; with some typical strengths of resonances important in nuclear astrophysics shown in Table 2-2. To estimate a typical resonance yield expected in SECAR, a resonance energy $E_r = 200$ keV, a resonance strength $\omega\gamma_r = 100$ meV, an energy-loss $\varepsilon_r = 10^{-13}$ eV·cm^2/atom, a reduced mass $\mu c^2 = 900$ MeV for mass 30, and $\hbar c = 197.3$ MeV·fm results in a typical yield on resonance of $2 \cdot 10^{-11}$ (one capture reaction in $5 \cdot 10^{10}$ incident beam particles). It should be noted, however, that some yields might be as low as 10^{-17} for some reactions. For this reason, SECAR is designed for a projectile rejection as high as 10^{17} with the separator and detection systems [2]. Separating the desired recoils from the unreacted beam is challenging since the beam intensities could exceed recoil intensities by 10^{17} and because the recoils and the beam differ by only one mass unit in (p,γ) capture reactions [8].

Direct measurements of capture reactions on stable target nuclei are usually made with a high-intensity proton or alpha beam on a thick target consisting of the heavy reactant. Once the light beam strikes the target, a capture reaction takes place and a germanium detector placed next to the target measures the γ rays resulting from the reaction. The recoils, or heavy products that are produced in the capture reaction, cannot directly be detected as they do not escape the target. The γ rays that are

Table 2-2: Predicted resonance energy and strength of the proton capture resonances on various beams to be used with SECAR [2].

Beam	Resonance Energy (keV)	Resonance Strength (meV)
^{22}Na	213	0.2
^{22}Na	610	600
^{23}Mg	486	38
^{25}Al	165	0.001
^{25}Al	412	18
^{27}Si	576	15
^{29}P	289	0.05
^{29}P	734	18
^{30}P	194	0.004
^{30}P	410	2
^{35}Ar	623	7

produced in the capture reaction can provide the needed reaction information, but γ-ray detection alone is not generally feasible with radioactive beams due to the high background from the decay of the beam. However, this heavy-target approach cannot be used with capture on most unstable nuclei as the lifetimes are so short that they usually cannot be made into a target [2]. To avoid these issues, SECAR will measure capture reactions in "inverse kinematics", using beams of radioactive nuclei incident on a helium or hydrogen gas target. This produces fusion capture reactions that then get filtered by velocity and momentum selection to eventually impinge upon a detector that measures the heavy recoils. Such an approach has already been successfully implemented for capture reactions at facilities such as the Detector of Recoils And Gammas Of Nuclear reactions (DRAGON) at the Tri-University Meson Facility (TRIUMF), the Daresbury Recoil Separator (DRS) at the Holifield Radioactive Ion Beam Facility (HRIBF) at Oak Ridge National Laboratory (ORNL), and with stable beams using St. George at the University of Notre Dame.

With DRAGON, the ^{21}Na(p,γ)^{22}Mg capture reaction was measured to improve nucleosynthesis models of the important NeNa cycle within novae, which is initiated by

radiative proton captures on ^{20}Ne. The nucleosynthesis in novae that occurs during the NeNa cycle creates the unstable ^{22}Na nucleus, which is extremely important astronomically as its beta decay leads to a potentially observable 1.275 MeV γ ray. ^{22}Na is created by the proton capture on ^{21}Na to ^{22}Mg, with a subsequent beta decay to ^{22}Na. The energies and resonance strengths for the most important resonances contributing to the ^{21}Na(p,γ)^{22}Mg reaction rate were studied in DRAGON at TRIUMF using inverse kinematics to detect the ^{22}Mg recoils via silicon-strip detectors at the focal plane [15]. The beam energy of 220 keV/A prompted the use of a Si detector for a total energy measurement of the recoils as it provides better total energy resolution than a gas ionization chamber at this energy.

Another successful study of capture reaction at ORNL was the ^{17}F(p,γ)^{18}Ne reaction that is important to both novae and X-ray bursts. Within novae, the β^+ decay of ^{18}F produces a positron which annihilates with other electrons, creating a large number of 511 keV γ rays that are potentially observable with γ-ray telescopes; however, the flux of γ rays depends on the amount of ^{18}F produced which in turn depends on the ^{17}F(p,γ)^{18}Ne reaction rate. In X-ray bursts the important ^{14}O(α,p)^{17}F(p,γ)^{18}Ne(α,p)^{21}Na reaction sequence initiates the α-p process and depends on the ^{17}F(p,γ)^{18}Ne reaction rate. The cross section of this reaction was studied with the DRS where the ^{18}Ne recoils were detected in a gas-filled ionization chamber [22]. The relative energy-loss versus total energy plot of this experiment is discussed further in Chapter 5. The beam energy of 637 keV/A prompted the use of an ionization chamber instead of a Si detector since the relative energy loss provides a determination of atomic number *(Z)* at this energy.

Observations from cataclysmic variables are useful in tandem with theory, but data-driven simulations are required to fully understand the underlying stellar properties and processes that observations cannot detect. The experiments at TRIUMF and ORNL have impacted the nucleosynthesis modeling of novae and X-ray bursts by studying

pertinent reaction rates with capture reactions and successful recoil separation. The successful study of capture reactions possible with SECAR will further improve our understanding of the evolution of cataclysmic variables and the nucleosynthesis occurring within.

CHAPTER 3. FOCAL PLANE BEAM PROFILE

Despite very high discrimination of the scattered beam particles from the fusion reaction recoils through electromagnetic separation, the recoils will not be the only particles reaching the focal plane. This mix of particles could be dominated by the unreacted beam particles with up to 10,000 unreacted particles to 1 fusion product [2]. Both the fusion products and unreacted particles arriving at the focal plane will have made it through the velocity filters and dipole magnets. An ion-optical simulation of the beam trajectory for a given initial energy and angle as it travels through SECAR is shown in Fig. 3-1. The key difference, and the difference that will allow their discrimination upon detection, is that the reaction recoils will have a higher mass, and thus lower velocity and kinetic energy, than the unreacted beam particles. The unreacted particles may not be the only undesired ions present. If the beam is not pure, reactions on contaminant ions can produce recoils with similar velocity and momentum as the beam, providing a particularly dangerous background that must rely on discrimination through techniques such as a relative energy-loss measurement. The detectors within the SECAR focal plane will be positioned relative to the ion-optical focus, which is 2.86 m downstream from center of the last quadrupole magnet (Q15), corresponding to a distance of 2.53 m from the beginning of the focal plane adapter to the focus.

Ion optics simulations show that a key feature of the beam at the focus is that it is dispersed more horizontally than vertically. This can be seen in a calculated cross section of the beam at the ion-optical focus from a Monte Carlo simulation as shown in Fig. 3-2 for a ^{21}Na(p,γ) experiment at an energy of 6.3 MeV (0.3 MeV/A) [23]. The initial energies and angles are sampled based upon realistic conditions for the reaction kinematics, taking energy loss in the target into account, and an ion optics simulation of trajectories was performed using the theoretical SECAR field maps. The spatial dispersion of the beam increases after the focus. As can be seen from Fig. 3-2 and 3-3,

nearly all the recoils at the focus are within a 2 cm diameter area. However, at the location of the stopping detector (about 21 cm downstream of the focus) the horizontal size of the recoils has increased to a little more than 3 cm. This horizontal dispersion is important for setting the location of the slits around the focus that will block some of the beam from entering the stopping detector, as well as the size and orientation of the MCP's foil (discussed further in chapter 5).

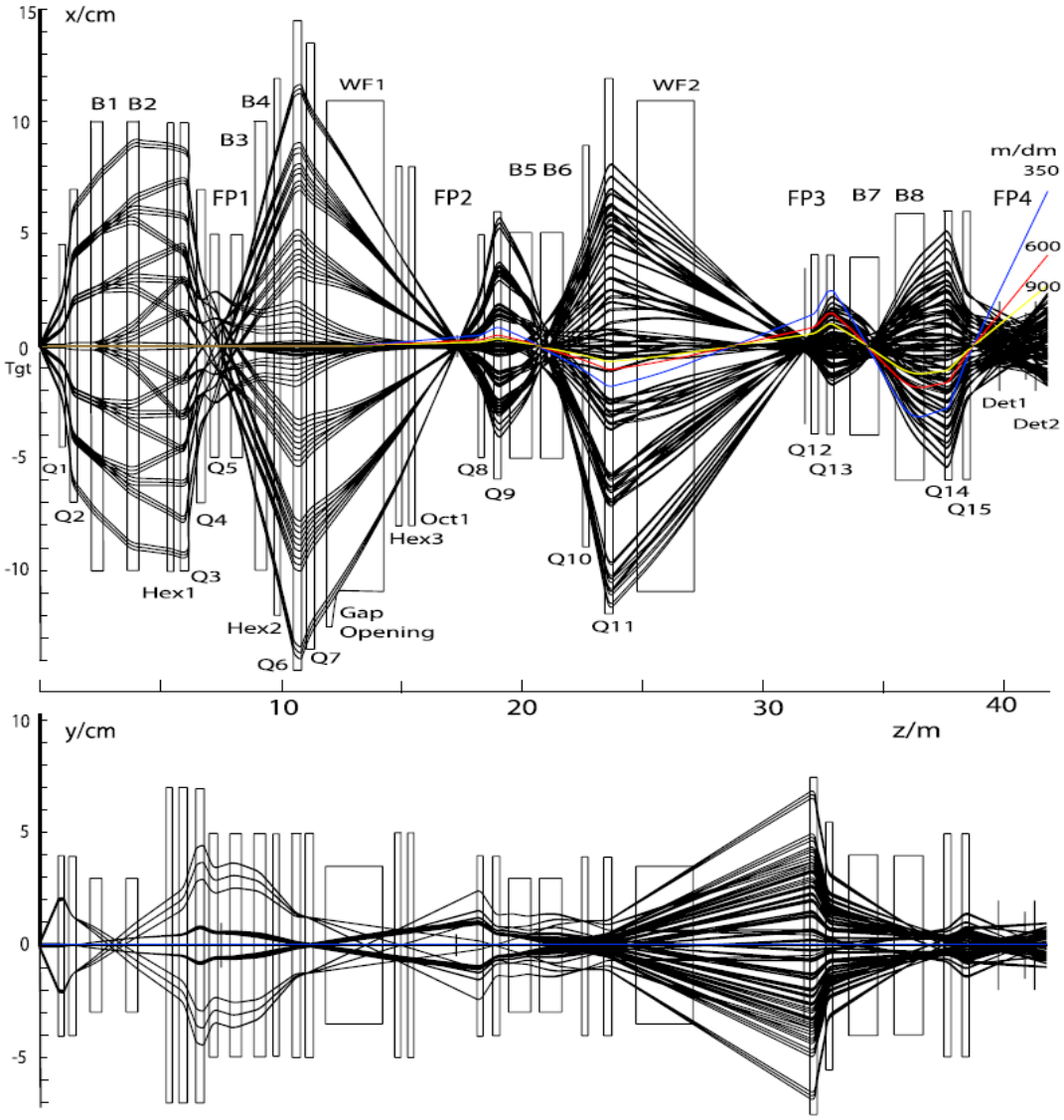

Figure 3-1: Ion optics of the beam through SECAR. There are 189 characteristic rays in the horizontal and vertical planes in upper and lower panel, respectively. The focal plane, with the MCP detectors and stopping detector, is located at FP4. In addition to the characteristic rays, rays representing mass resolving powers of 350, 600 and 900 are shown in blue, red and yellow respectively [24].

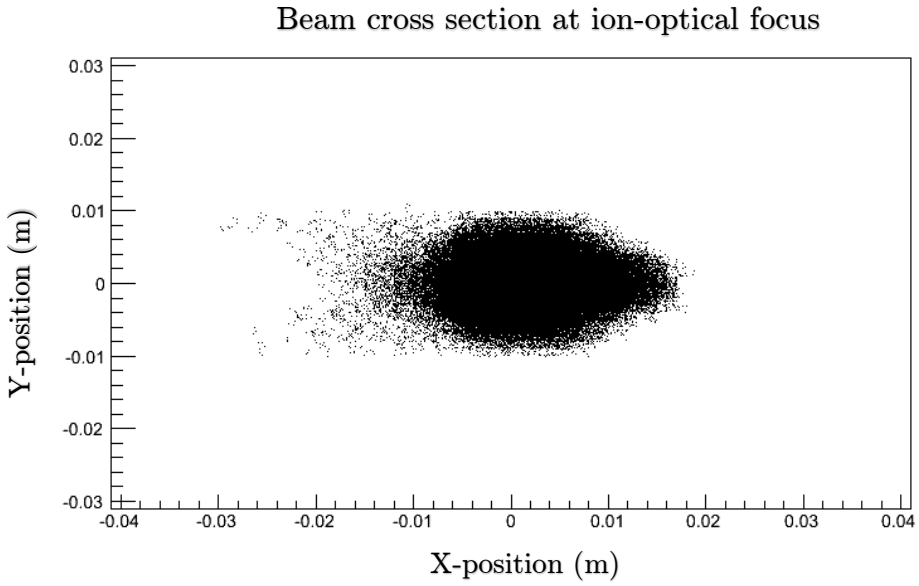

Figure 3-2: Cross section of the beam at the ion-optical focus [23].

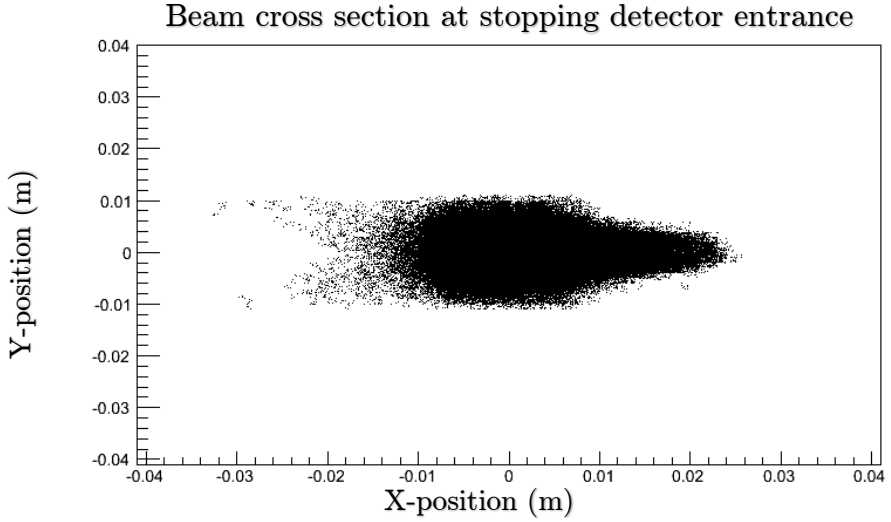

Figure 3-3: Cross section of the beam at the entrance of the stopping detector (Ion chamber or Si detector). Notably the spread in the x-direction is much larger than the vertical dispersion [23].

The use of slits to block the beam within SECAR differs from its use in experiments as those using tagging spectrometers, where the analysis of data is not hindered if the slits block some of the recoils of interest so as to not include a significant

background at the final focal plane. In SECAR, all of the recoils of a selected charge state should arrive at the focal plane to improve statistics and the efficiency determination that enters into the total cross section. The slit system will therefore be inserted for tuning and diagnostic purposes and then positioned in an experiment appropriately to ensure no recoils will be blocked [2].

Fig. 3-4 shows the number of recoiling ^{22}Mg nuclei as a function of position from the ^{21}Na(p,γ) reaction for both the intensity versus positon at the ion focus location and the entrance to the ion chamber. The majority of the particles are tightly grouped within a 2-3 cm diameter. A larger detector is required to collect the small number of particles further from the center of the beam, in the "tails" of the histograms.

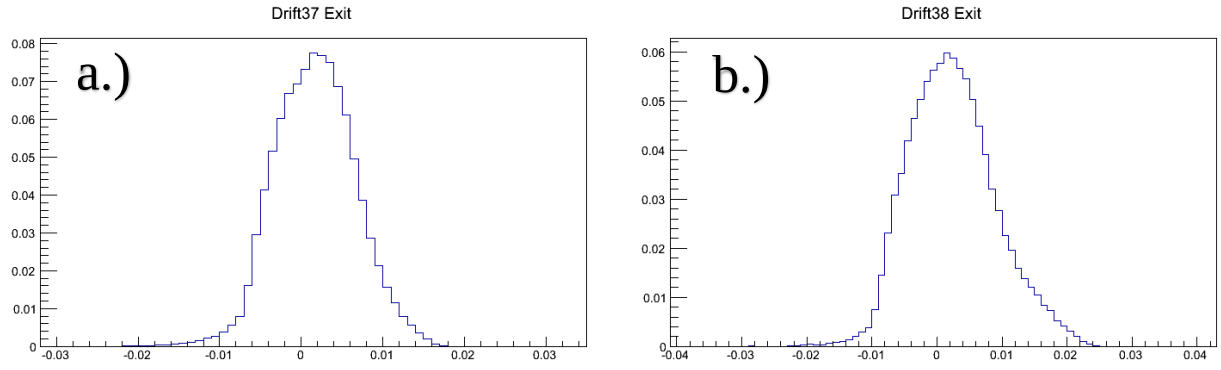

Figure 3-4: Histograms for the relative intensity of the beam as a function of its horizontal position at a.) the ion chamber entrance and b.) the ion focus [23].

CHAPTER 4. FOCAL PLANE CHAMBERS AND INFRASCTRUCTURE

This chapter addresses the design of the focal plane chambers and their stands to meet specifications for the location of the ion-optical focus, the initial suite of instruments, as well incorporating the overall goal of flexibility for future development and adapting to different experimental conditions. Initially, the focal plane will house two micro-channel plate (MCP) detectors and a stopping detector of either a gas-filled ionization chamber or a silicon strip detector.

To accommodate these detector systems, as well as future instrumentation, the chambers of the focal plane are designed with multiple access ports for flexibility. Standard flanges are used to minimize cost and increase adaptability. The size of the focal plane chambers is optimized to allow for full acceptance of the recoil beam envelope without being superfluously large. The focal plane chambers are supported on two separate steel stands. The longer stand located upstream supports chambers housing the time-of-flight detectors while the shorter stand downstream supports the diagnostics box and the stopping detector.

The focal plane chambers and support structure, shown in Fig. 4-1 and Table 4-1, house the detectors responsible for the discrimination and measurement of the recoils. Measurements using beams with a wide range of conditions (mass, energy, purity) are expected given the range of the SECAR experimental program. Since no one approach is best suited to all these conditions, a guiding principle of the focal plane design is to provide flexibility to optimize the configuration to the beam conditions of any given experiment.

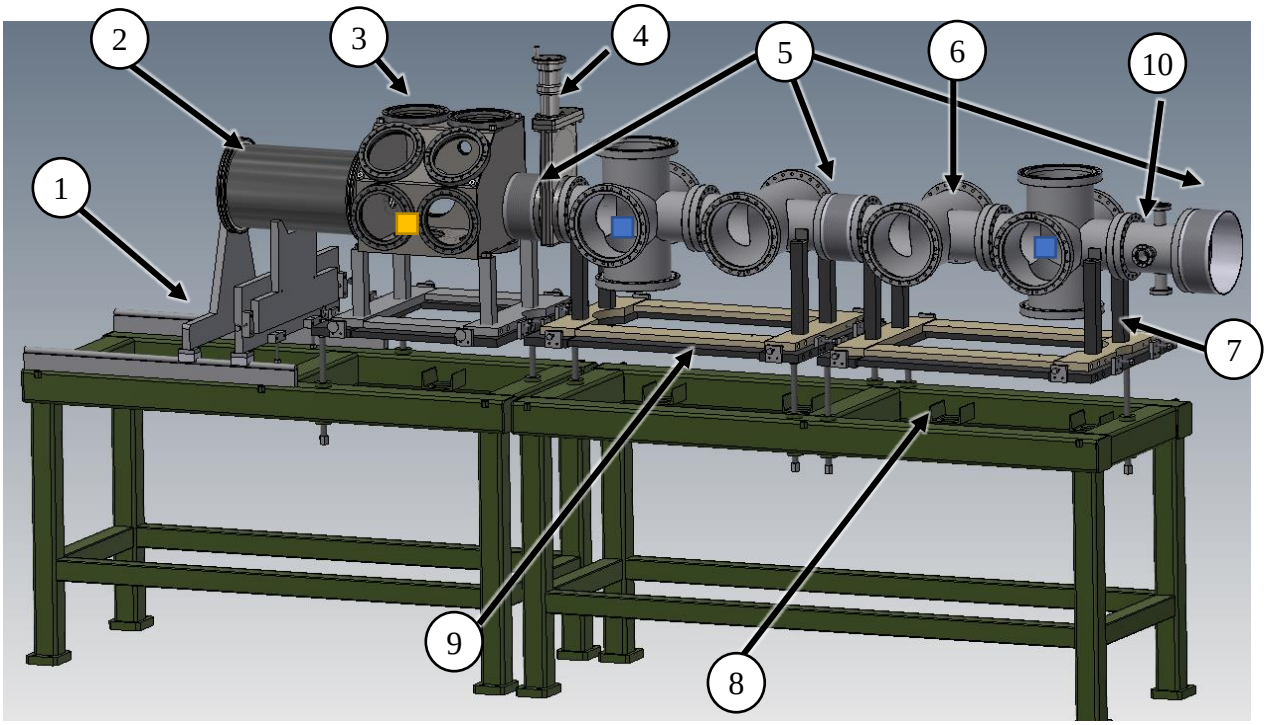

Figure 4-1: Isometric schematic of SECAR focal plane chambers with numbered part list described in Table 4-1. Ion-optical focus approximate location within the diagnostic box is denoted with a yellow square. Approximate MCP locations within the 6-port chambers are denoted with blue squares.

Table 4-1: List of parts within SECAR focal plane.

Number	Part Reference
1	Ion Chamber Rail system and support
2	Ion Chamber
3	Diagnostic Box
4	Vacuum Valve
5	84 mm-112 mm Adjustable Bellows
6	4-port and 6-port chambers
7	Aluminum Vertical Support
8	U-channel Tie-down tabs
9	Planar Adjustable Plates
10	Upstream 8” to 6” adapter

Beyond the excellent discrimination from charge-to-mass *(q/A)* selection created by a combination of velocity and momentum separation, the recoils can also be discriminated from the beam using several approaches: the relative energy-loss (ΔE-E) of an ion as it transverses through the gas of an ion chamber, the total energy of the ion, and the time-of-flight of the ion. Ideally, the best discrimination comes from a combination of all of these techniques, but in reality, the relative energy-loss (ΔE-E) works best for fast and light ions, while time-of-flight works best for slow and heavy ions.

The focal plane is designed so that the focus falls inside a diagnostics chamber where slits and a variety of diagnostics will be located. With all the bellows at their midpoint (relaxed) length, the focus is 0.36 cm upstream from the center of the diagnostics box. The upstream connection of the focal plane to the rest of SECAR is shown in Fig. 4-2 and shows the location of the ion-optical focus from the center of the last quadrupole magnet (Q15). The location of the focus and the lengths of the focal plane chambers are shown in Fig. 4-3.

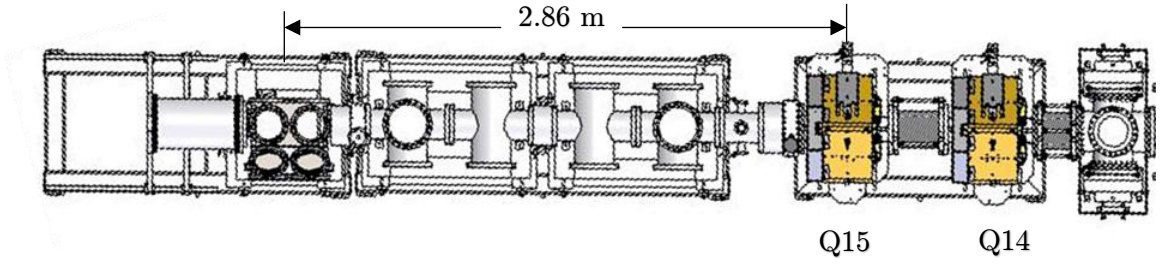

Figure 4-2: Top view of the focal plane connected to the last quadrupole magnets in SECAR. The quadrupole magnets Q14 and Q15 are shown. Q15 is connected to the focal plane adapter by a vacuum gate valve. Dimension shown (in meters) is given length from the center of Q15 to the location of the ion-optical focus.

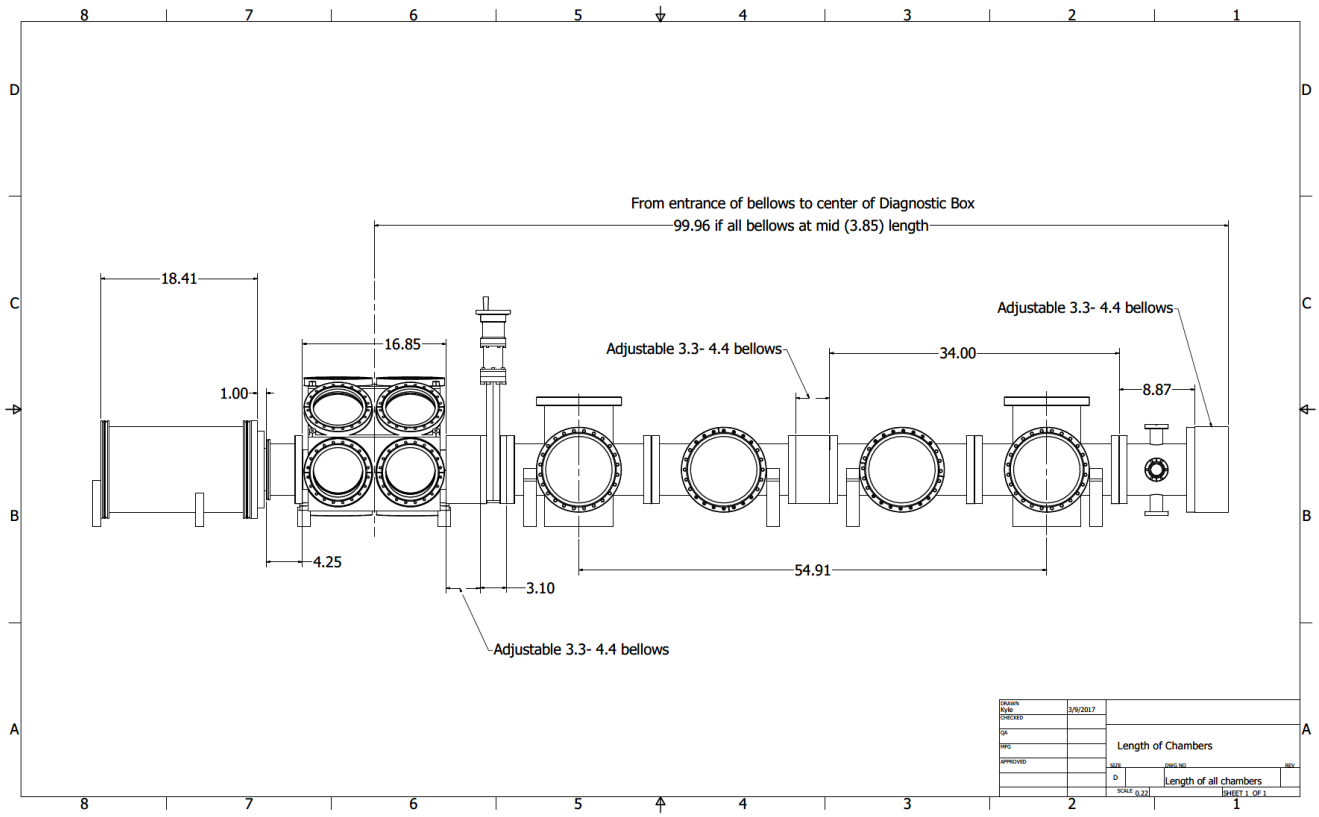

Figure 4-3: Side-view drawing of focal plane chambers that the beam will travel through to show relative lengths. All shown dimensions in inches.

4.1. Time-Of-Flight Section

The time-of-flight section, shown in Fig. 4-4, is built to support two sections, each with their own independent adjustment plates. Both sections contain identical 4-way and 6-way crosses, but with the order reversed, with the 6-port chambers being on opposite ends. The steel stands are generally designed similar to other stands within the SECAR beamline, following the same dimensions for the height and width. The chamber lengths upstream from the focus are chosen to maximize the time-of-flight measurement with a pair of MCP detectors housed in 6-port chambers at a distance apart of 139 cm along the beam axis between the two detectors. A MCP detector (described in more detail in chapter 5) consists of a thin foil centered in the beamline

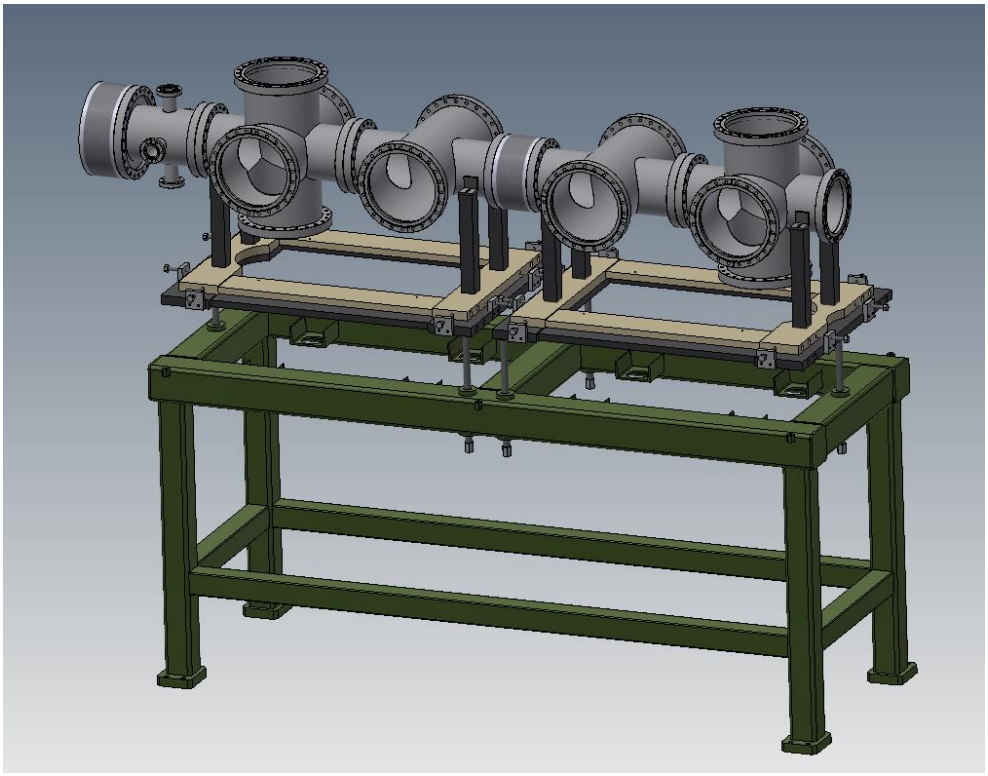

Figure 4-4: Longer steel stand supporting mirrored chamber and planar adjustable plate setup with adapter facing upstream. Adjustable bellows connects the 4-port chambers.

which, upon impact, will release electrons to be collected by an MCP. Each MCP's thin foil is placed at the center of its 6-port cross chamber. A MCP detector, electric field grids, and magnets are mounted on the top flange of its 6-port chamber. The foil and accompanying electric field grids are mounted on one of the horizontal ports perpendicular to the beam axis, with a viewing window on the opposite horizontal port. One of the 4-port chambers houses a pumping station and gauges while the second 4-port chamber is not instrumented initially but could be used for other future diagnostics.

A 3-point support design is implemented for the chambers that allows for leveling and a ± 3" vertical adjustment around the beam axis while eliminating the unnecessary constraint that a four-post support would have. The long steel stand has six 2" holes drilled through the top beams in two mirrored triangular patterns where tapped steel

inserts will be welded in the cavities. These steel inserts have 3/4"-16 sturdy tapped rod inserted into them with a spherical washer on top of the rod to fit into a dimple on the lower aluminum plate. An exploded view of the long stand with steel inserts and threaded rods is shown in Fig. 4-5 while the spherical washer connecting to the lower plate is shown in Fig. 4-6. Lastly, the stand has two sets of four steel U-channels welded into the inside of the stand which will be used as a tie-down for the aluminum plates held up by the spherical capped steel rods.

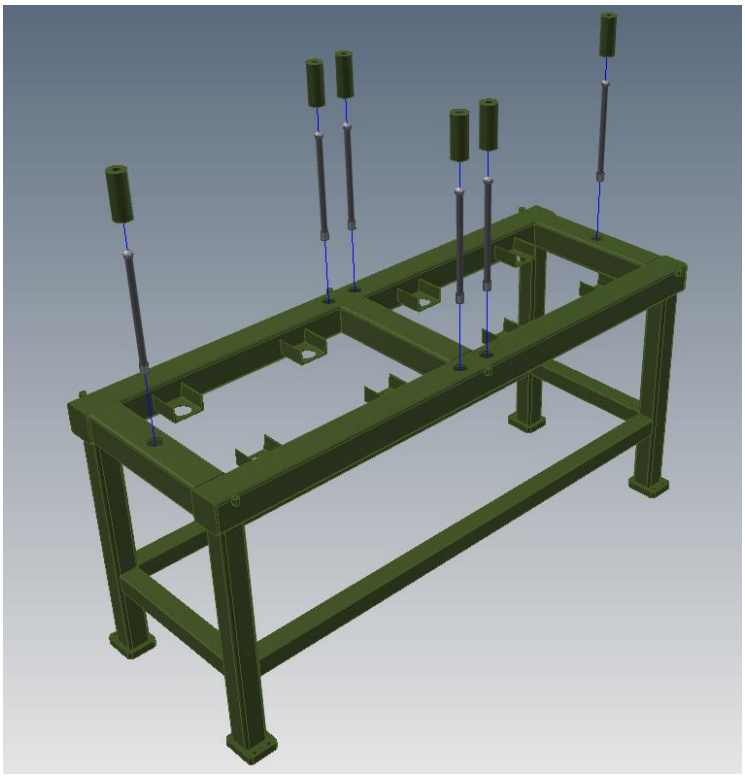

Figure 4-5: Exploded view of the long steel stand with threaded steel inserts and threded rods that will hold up the slidable plates.

Two layers of aluminum plates are implemented to allow for horizontal adjustment, they consist of a lower and upper plate, where the lower plate sits on the spherical washers on the steel support rods, and the upper plate slides in two dimensions in a horizontal plane across the lower plate. The upper and lower plate assembly can be

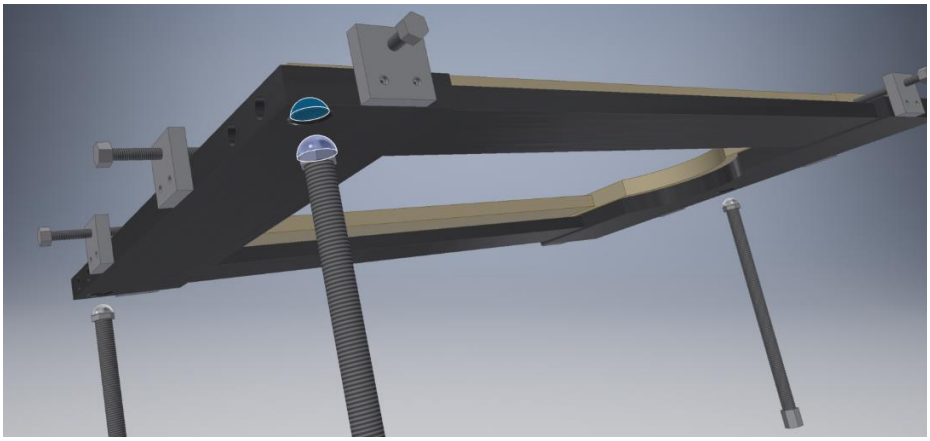

Figure 4-6: Close-up of how the adjustable plates are supported with the spherical washer capped rods in a triangular pattern. The spherical cap fits into a dimple on the bottom of the lower plates.

seen in Fig. 4-7 where the lower plates are colored dark gray and upper plates beige. Both the lower and upper plate assemblies consist of four separate aluminum plates bolted together into a hollow rectangle, with the lower assembly being larger. For both the upper and lower plates, the longer plates along the beam axis have smaller thickness than the end plates. This is so that when the upper plate assembly slides across the lower, only the end pieces will be in contact, reducing the friction in sliding. In addition, this design requires only the end plates to be parallel reducing the constraints on flatness and parallelism, simplifying assembly.

The lower plates have two aluminum blocks attached to each side (8 in total) with a height that extends to the top of the upper plates. These blocks have one 3/8" - 16 tapped hole where a jack screw will be located to push against the top plates. These jack screws push the top plates to slide in a horizontal plane and allow for finely-tuned alignment. The jack screws allow for a movement of ± 3/4" in the direction perpendicular to the beam axis, denoted as the y-direction in Fig. 4-8. The other push screws allow for a ± 1" movement in the direction parallel to the beam axis, denoted as the x-axis.

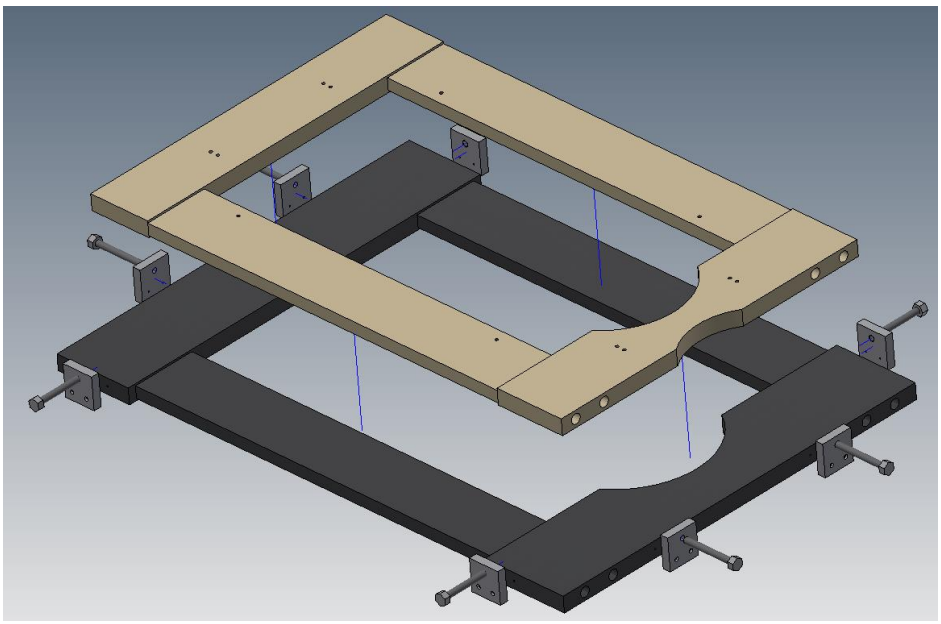

Figure 4-7: Isometric view of how two sets of aluminum plates, upper (beige) and lower (dark gray), lay on top of one another. The upper plate can slide on top of the lower plate.

The top plates have four pairs of counter bored holes, two pairs on each end plate, that connect to four aluminum vertical pillars that support the steel vacuum chambers. These 11" tall aluminum supports are shimmed to the correct height to connect to a 90-degree steel tab which is welded directly to the vacuum chambers; an exploded view of this assembly is shown in Fig. 4-9. The adjustable plates have a semicircular hole on the inside of one end that allows for clearance of the vertical port on the 6-port chamber, which makes internal access much easier. Different supports (e.g. of another height or location) could be implemented with new mounting holes and supports in the top plate if alternate chambers were desired for future detector systems.

Each section consists of a 4-port chamber connected to a 6-port chamber. The ports on the 4-port chamber have a 6" outer diameter standard tube (DN160 CF flange) along the beam axis with 8" outer diameter standard tube (DN200 CF flange) for access

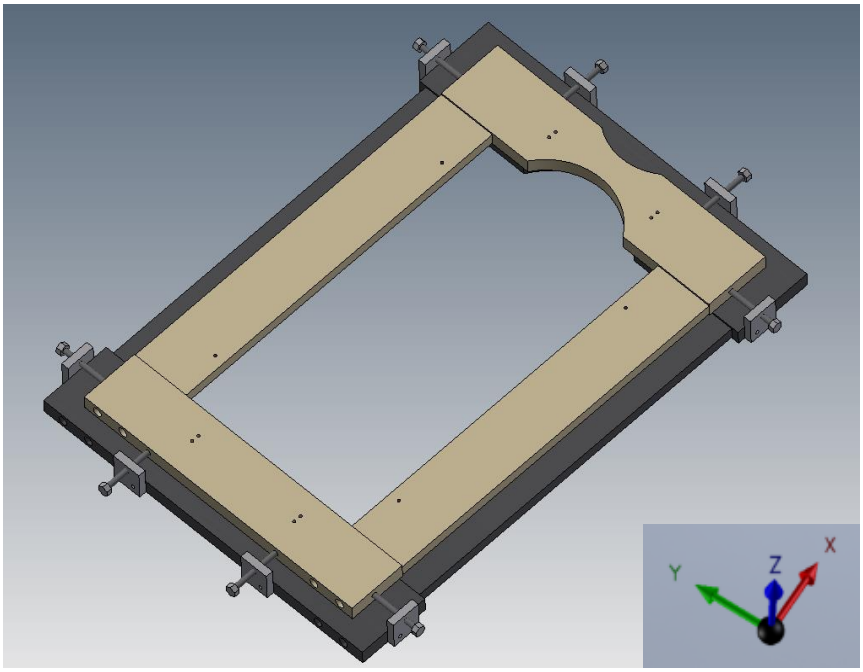

Figure 4-8: Isometric view of the two layer sliding plates. The x-axis points along beam axis and z-axis points vertically. Movement of upper plate is in x-y plane.

to the ports facing horizontally. The 4-port chambers can be oriented vertically instead, but this restricts the access to the downward facing port by the aluminum plates. It is likely that the 4-port chamber that houses one of the pumping systems will be oriented vertically and the downward facing port is not planned to be instrumented initially and will be blanked off. The 6-port and 4-port chambers will be connected along the beam axis by the smaller (DN200 CF) flanges. The 4-port and 6-port cross chambers, which are held up with the aluminum pillars on the adjustable plates, attach to an identical but mirrored setup via an adjustable (84 mm to 112 mm in length) bellows, allowing for flexibility in both the connection and overall length. The positions of the chambers are ordered with the two 4-port chambers closest to each other and is chosen such that the 6-port chambers that will house the MCP detectors are a maximum distance apart from one another to get the largest time-of-flight possible.

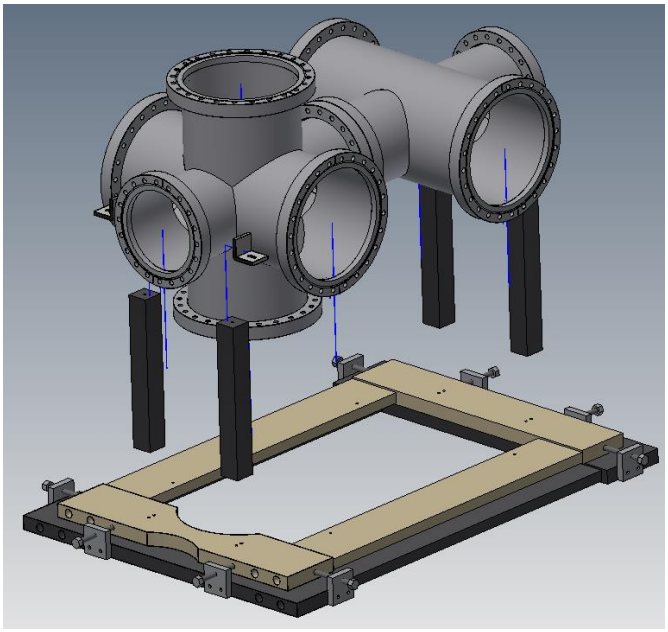

Figure 4-9: Exploded view of the connections between the adjustable plates, the aluminum vertical pillars, and 4-port and 6-port chamber system.

4.2. Diagnostics and Ion-Chamber

The shorter of the steel stands is downstream from the longer steel stand and supports the diagnostic box on its own adjustable planar plates, as well as the ionization chamber and its rail support system. As seen in Fig. 4-10, a vacuum valve (yellow) and an adjustable (84 mm to 112 mm) bellows (orange) connects the downstream 6-port chamber on the long stand to the diagnostic box and ionization chamber on the short stand.

The ionization chamber utilizes a rail system for removing the back end of the housing for maintenance, or the removal of the entire ion chamber for substitution of the window to the ion chamber to match the beam conditions and ion chamber pressure. This rail system also allows for quick substitution of pre-aligned instrumentation in place of the ionization chamber if this is required by an experiment. The design of the cradle for the ionization chamber includes a preliminary vertical and horizontal

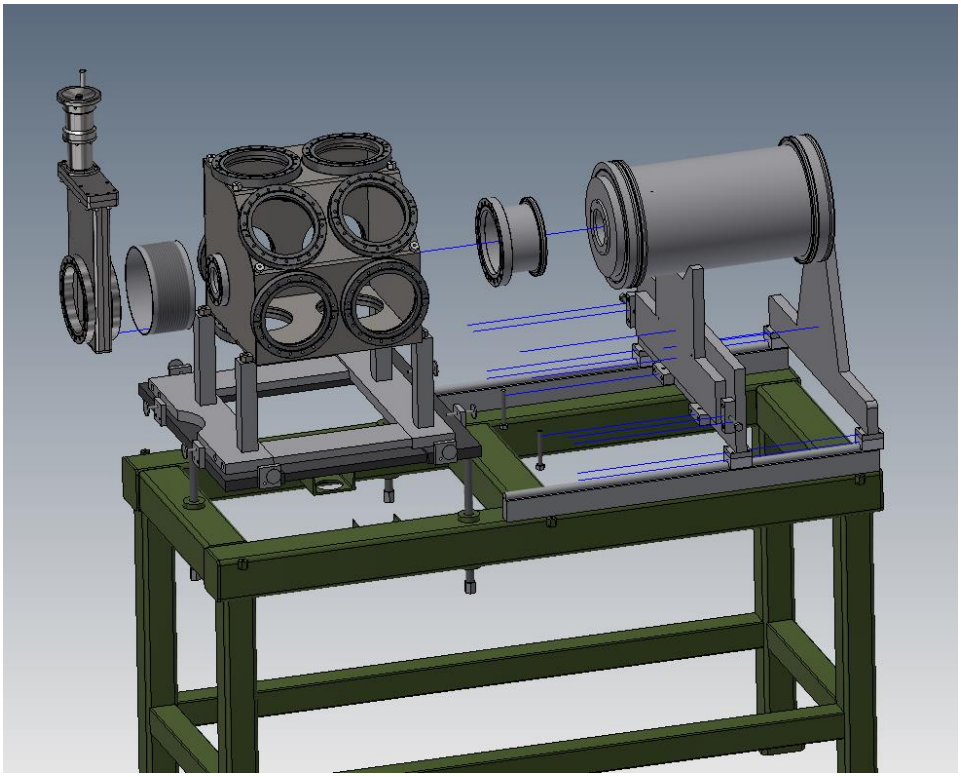

Figure 4-10: Isometric view of the Diagnostic box, its slidable plates, and the ionization chamber supported by the short stand.

adjustment capability with a plate that holds the ion chamber being able to slide across the plate that is connected to the rails.

The diagnostic box and ionization chamber will frequently be manipulated during experiments, and the vacuum valve separating the chambers from the diagnostic box allows the moisture sensitive MCP's to remain in the vacuum-sealed chambers while this happens. A slit system is placed in the diagnostic box just upstream from the focus that will have horizontal and vertical slits to help stop leaky beam from reaching the ionization chamber. The multiple ports of the diagnostic box serve many functions, including a connection for a pumping station. The housing of a Faraday cup, a segmented beam-centering monitor, and a low intensity diagnostic are contained inside the diagnostic box, which has numerous ports to accommodate additional diagnostics or future modifications.

A shorter steel stand supports the ionization chamber and diagnostics box. The short steel stand contains the same vertical adjustment approach using three vertical 3/4”-16 support bolts like the long stand, which hold up a similar planar adjustable plate setup. However, here the adjustable plates are shorter in length and do not require a semi-circular hole for an access port. The aluminum vertical pillars that attach to the top plate here are also like those that hold up the chambers in the long stand, but are a shorter height.

CHAPTER 5. MICRO-CHANNEL PLATE DETECTOR

The detectors at the focal plane must provide a high discrimination between the desired capture reaction recoils and the other background ions. This section describes the design of the first detector that the ions will encounter in the focal plane; the micro-channel plate (MCP) detectors provide high resolution timing and position measurements. The micro-channel plate detectors are position-sensitive timing detectors that are well suited for detecting low-energy heavy ions with minimal effect on the ion's trajectory. SECAR's focal plane uses two MCP detectors for a time-of-flight measurement of the particles due in part to the MCPs' excellent timing resolution. The desired recoils have a slightly greater mass than that of the unreacted beam, but also a lower velocity; meaning the discrimination of these species can be accomplished by accurately measuring the time they take to travel between the two MCPs. The design of the MCPs to be utilized in SECAR is based upon the design of Shapira *et al.* [25], which demonstrated excellent position (~1 mm) and timing (~1 ns) resolution, and tolerance of high rates (up to 10^6 particles per second).

The MCP layout, shown in Fig. 5-1 uses a single metalized foil, tilted 45-degrees from the horizontal plane of the beam axis to allow the beam to pass through the foil relatively uninhibited. As seen in the cross sections in Fig. 3-2 and Fig. 3-3, the recoils are more spatially dispersed horizontally. Tilting the foil in this orientation maximizes horizontal acceptance and allows all of the recoils to pass through. The emitted secondary electrons following the heavy ion impact are then accelerated through a potential difference on the order of 100V by a grid of thin, high-voltage wires that accelerate the electrons towards the MCP detector. To help guide these electrons, which can start out with significant transverse momentum, a permanent magnet is placed behind the detector, causing the electrons to move in a spiral motion along the magnetic field lines to the MCP detector, as shown in Fig. 5-2. A calculation of the magnetic

focusing shows that for a 12,300 Gauss permanent magnet located a distance of 2" behind a 40 mm diameter MCP, and the foil a distance 4.68" from the MCP, relates to a magnetic image magnification of 0.48. This means that for a 40 mm diameter MCP, a 84 mm foil can be used to effectively capture all of the secondary electrons. The 45-degree orientation of the foil gives a 84 mm horizontal acceptance, but a 60 mm vertical acceptance.

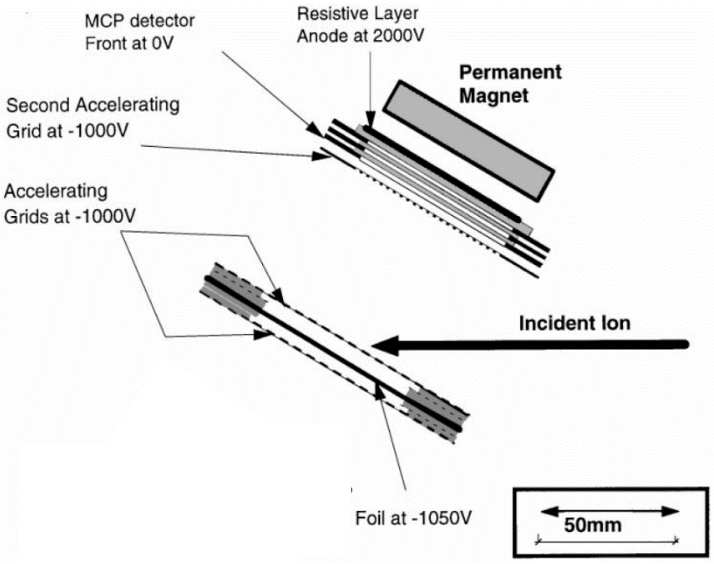

Figure 5-1: A schematic showing the orientation of the MCP as well as the foil the beam will be incident upon [25].

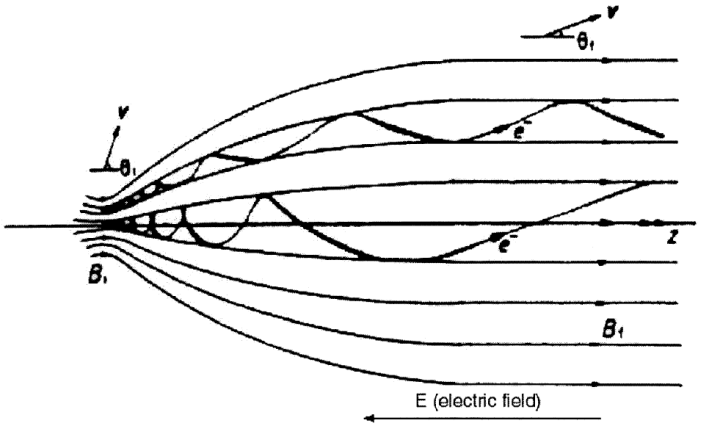

Figure 5-2: A diagram showing the helical motion of the secondary electrons towards the MCP, influenced by magnetic and electric fields [25].

The MCP detector, shown in Figs. 5-3 and 5-4, consists of two electron-multiplying micro-channel plates stacked on top of each other. The plates are a thin (~5 mm) ceramic material with an array of tubes with diameters of approximately 12 μm a slight angle (~10°) from the normal to the surface. These electron-multiplying plates are stacked on one another with opposite angles of the tube arrays. The pulse of the initial electron entering a channel, and its subsequent electron multiplication, strikes a resistive anode plate that has four electrical contacts at the edge, spaced 90-degrees from each other. The position is determined by comparing the magnitude of the signals from the four contacts, since this magnitude depends on the path resistance [26]. Two such signals from opposite ends of the MCP outputs are shown in Fig. 5-5 from initial testing at LSU with alpha particles of a ^{241}Am source.

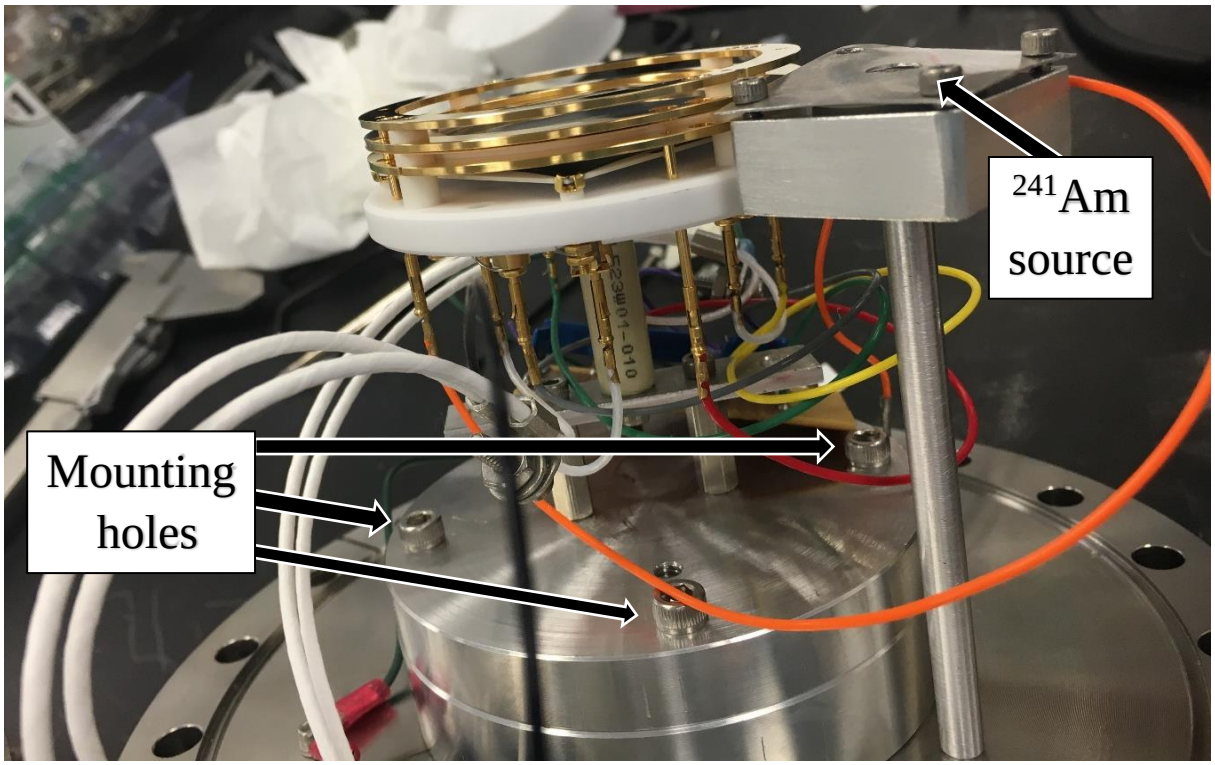

Figure 5-3: The MCP, and its wiring, mounted on test flange at LSU. The ^{241}Am source emits alpha particles incident on a metal-foil in the test chamber.

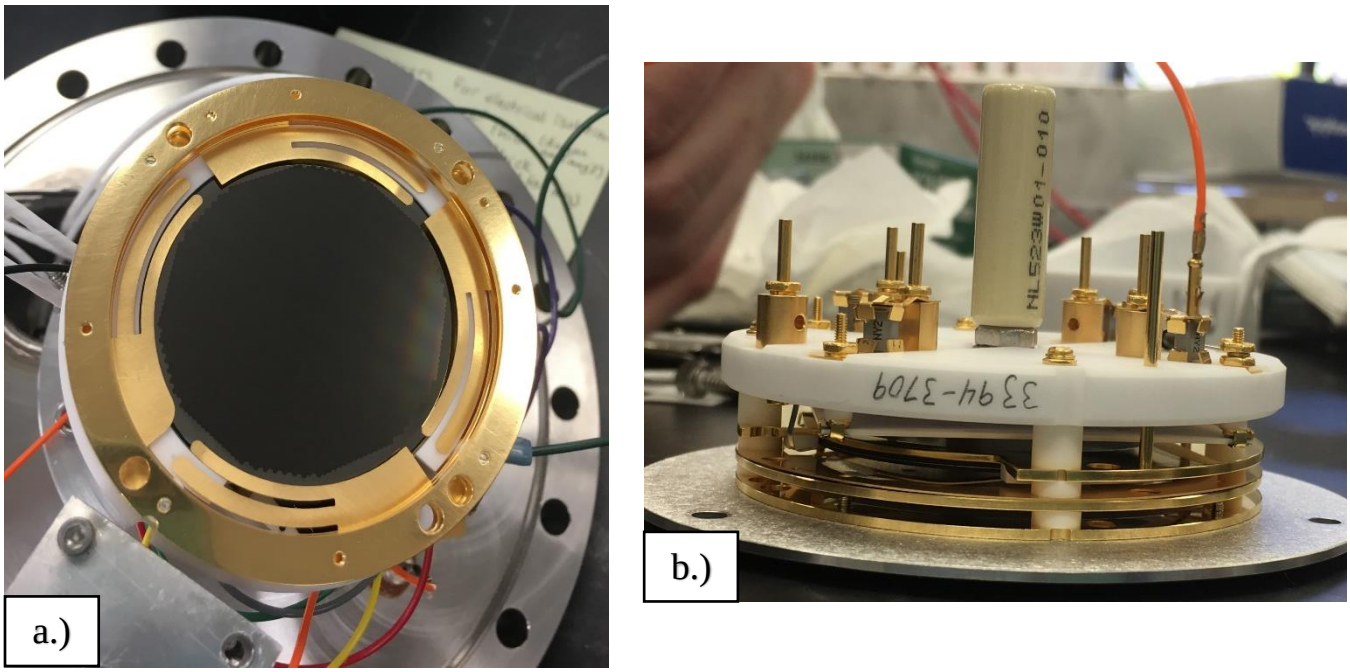

Figure 5-4: a.) Top view of the 40 mm diameter MCP on test flange. b.) Side view of MCP prior to mounting and wiring.

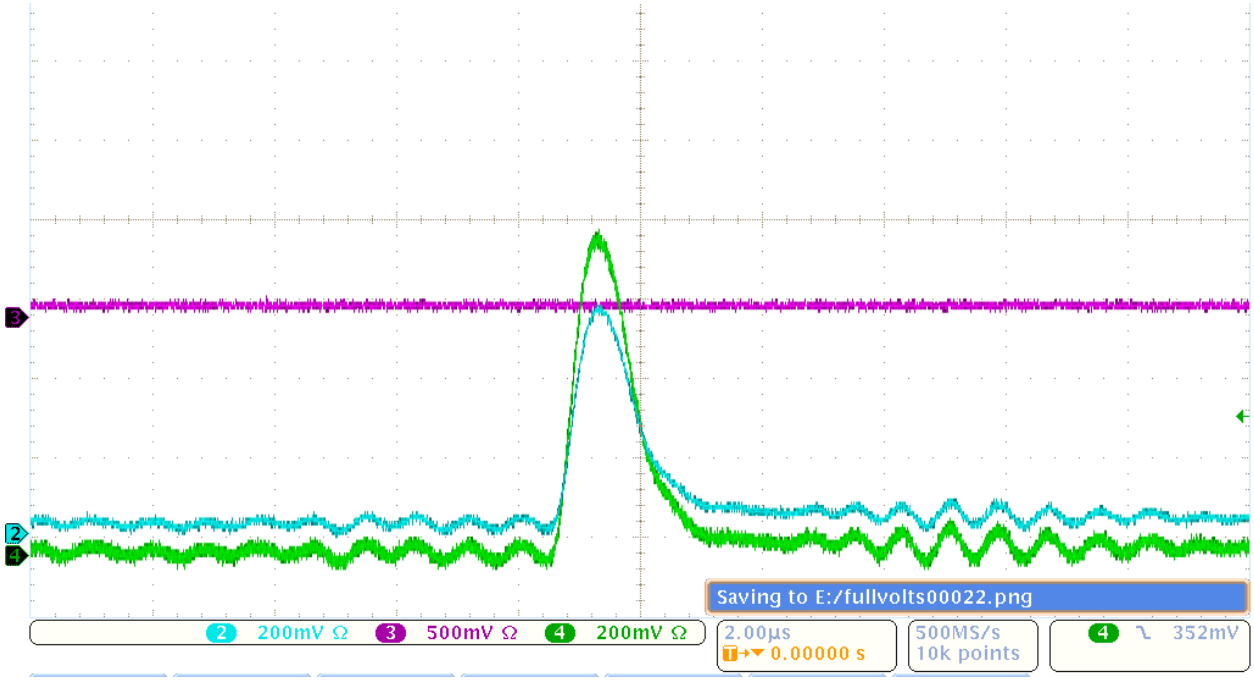

Figure 5-5: Signal from two (opposite) sides of the resistive anode of the MCP. The relative amplitude of the pulses will be used to determine the position.

The first MCP the ions encounter in the focal plane will be positioned 21.3" from the entrance of the upstream bellows, which is 78" upstream from the ion-optical focus, and measures the position of the ions as they enter the focal plane chambers in addition to initiating the time-of-flight measurement. The second MCP is positioned 54.9" downstream from the first and works with the first MCP to give a time-of-flight measurement for the ions. Additionally, the position on the second MCP allows a trajectory measurement of the ions that can be used to improve time-of-flight and provide additional discrimination since trajectories of the recoils and leaky beam may be different. The MCPs are positioned before the optical focus so that the stopping detector (gas ionization or silicon strip detectors) can be placed close to the optical focus to reduce the detector size and ion divergence [2]. The flange mount that the MCPs are attached to inside of the 6-port chamber is shown in Fig. 5-6. The metal-foil (not shown) is mounted on one of the side ports such that the foil is in the path of the beam and parallel to the plane of the MCP.

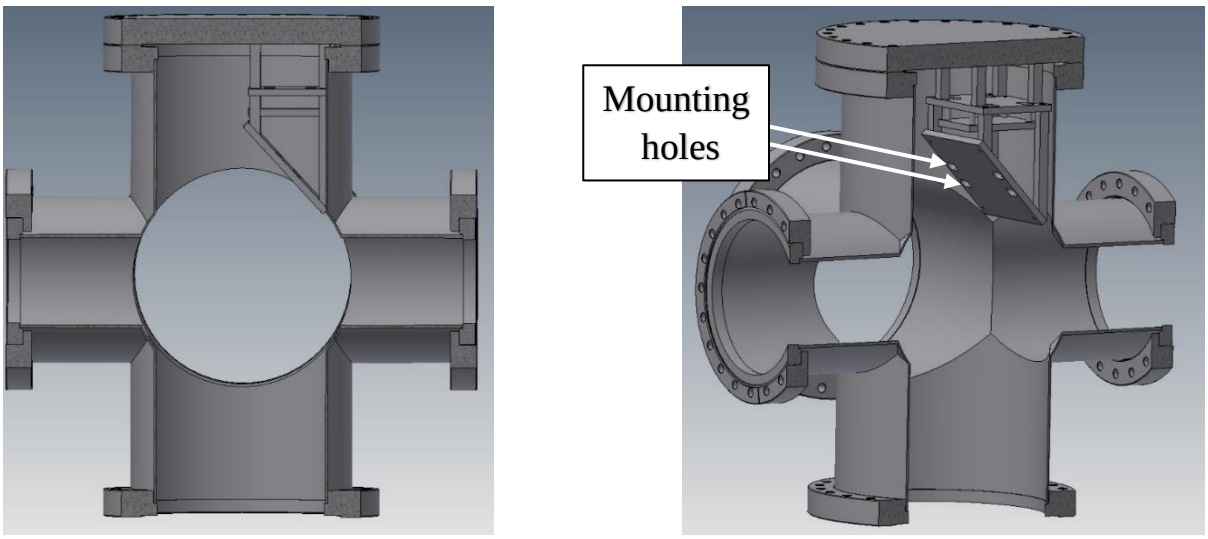

Figure 5-6: Side and Isometric cross section views of the MCP mount from the top flange inside the 6-port chamber. The MCP and permanent magnet (both not shown for clarity) mount on the 45-degree plate. The beam axis is through the smaller (8") horizontal ports. A retractable mount for the metal-foil will be placed on one of the larger (10") horizontal ports.

As an example of the time resolution capabilities of the MCPs with the typical energies used in SECAR, a beam of 0.2 MeV/A has speed v/c ~2% and takes approximately 230 ns to travel between the two MCP detectors ~55" apart. Assuming ~1 ns individual MCP timing resolution, this corresponds to a relative resolution ($\delta t/t$) of approximately 0.6% in a time-of-flight measurement between the two MCPs. This should be compared to the relative time difference of ~2% expected from the difference in velocity between the beam and recoils, which is more than three times greater than the relative timing resolution. Thus, for the 0.2 MeV/A energy beam, the recoils can easily be resolved from the beam. For higher energy beams of 3 MeV/A, the recoils have a speed v/c ~8% and take approximately 58 ns to travel between the two MCP detectors. This relates to a time-of-flight resolution ($\delta t/t$) of about 2.4%, which is nearly identical to the difference in time-of-flight of the recoils and the beam, requiring an additional means of resolving the two. However, when higher energy beams give a time-of-flight relative resolution that cannot be easily resolved, a gas ion chamber provides better discrimination of ion species.

The MCP position resolution also improves particle discrimination in two ways. First, the incoming beam is mass-dispersed at the optical focus, meaning the trajectory measurements may allow the rejection of scattered beam not centered on the beam axis leaving the last quadrupole magnet Q15. Secondly, the position measurements allow a correction to the distance between the MCP's further improving the recoil time-of-flight resolution [2]. After their flight through the MCPs, the ions pass through the diagnostics box where the ion-optical focus is located. At this point slits are used to block leaky beam and can be adjusted accordingly by the trajectory measurements from the MCPs.

CHAPTER 6. FINAL STOPPING DETECTOR

After the diagnostic box, the ions are stopped by a gas ionization chamber or silicon strip detector. In the case of a gas ionization chamber, the ions enter the gas ionization chamber through a thin window (typically of mylar or kapton) and lose energy in ionizing the gaseous contents of the chamber. As stated previously, the desired recoils and the scattered beam have nearly identical momentum, but the energy of the recoils is slightly smaller. Additionally, the recoils and scattered beam differ in atomic number Z by only 1 (or 2) for the fusion (p,γ) (or (α,γ)) reactions. Furthermore, any beam contaminants that add to the background of the scattered beam typically have a lower Z than the beam and are easily discriminated in the ion-chamber.

The ionization chamber is typically filled with 50-500 Torr of isobutane (C_4H_{10}), which is ideal because of its low ionization potential of 10.8 eV and mean energy for ion-electron pair creation of 23 eV [27]. This results in the largest signal and best resolution for a given energy loss [28]. As the entering heavy ions are slowed in the gas, they ionize gas molecules, creating charged particles that are accelerated towards a cathode and anode. The electrons created in ionization drift relatively quickly in the electric field and can then be measured by means of the voltage they induce on three collecting anode sections, which is related to original energy of ionizing ion. A relative energy-loss measurement between the sections provides discrimination of the initial ion's atomic number from that of the beam. For example, a plot of energy-loss in the first section of the detector vs. the total energy in an ion chamber is shown in Fig. 6-1 for a resonance in the $^{17}O(p,\gamma)^{18}F$ reaction that was measured using the DRS, with the desired ^{18}F recoils denoted in the black circle [29]. The ionization chamber for SECAR uses this same relative energy loss measurement technique. For ion energies greater than around 0.5 MeV/A, the relative energy-loss (ΔE-E) that an ion experiences in the gas-filled chamber gives an accurate discrimination of the atomic number.

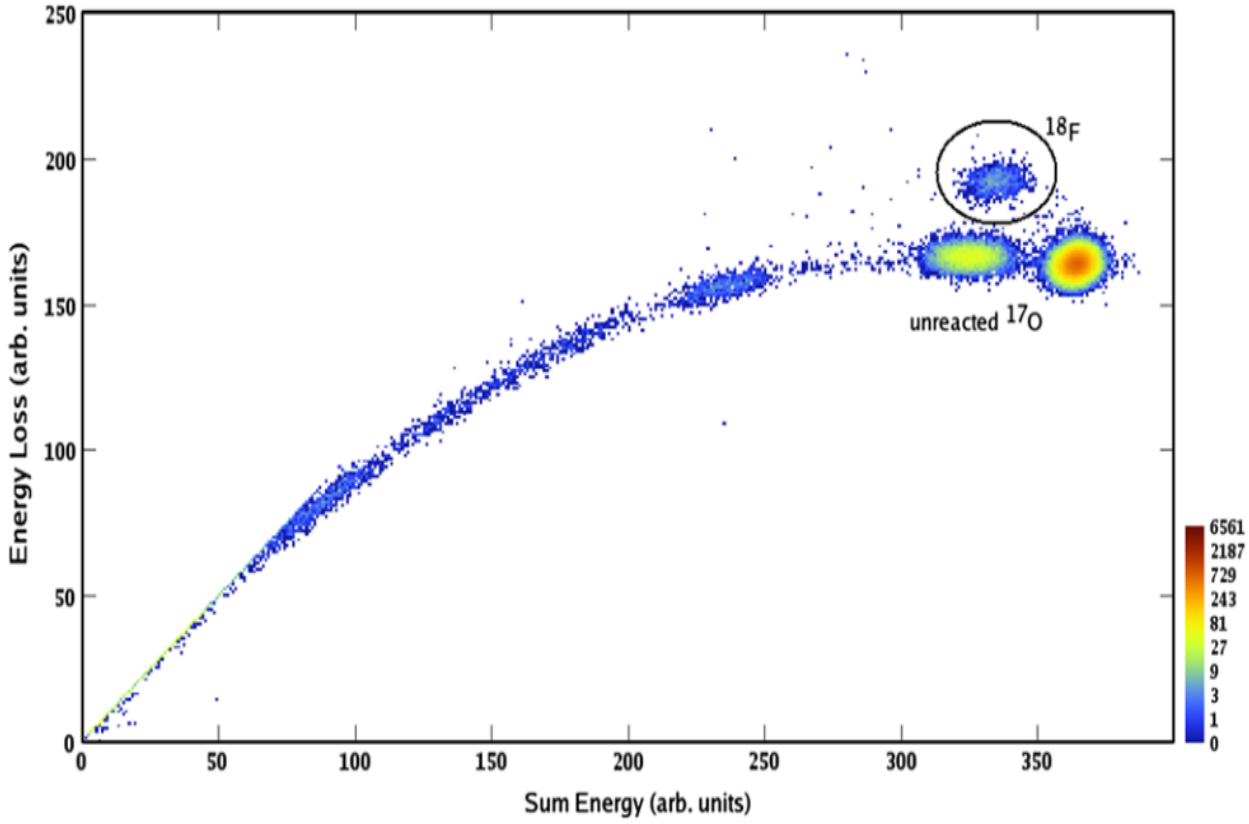

Figure 6-1: Energy-loss vs. Total Energy of particles as they travel through the ionization chamber for a 557 keV resonance in $^{17}O(p,\gamma)^{18}F$ [29].

The ionization chamber to be implemented in the SECAR focal plane has been designed and constructed at Louisiana State University. A CAD drawing of the initial design is shown in Fig. 6-2 and the constructed result is shown in Fig. 6-3. The design of the gas ionization chamber uses a standard cross-field ΔE–E design similar to the one in DRS [29] but augments it with a position-sensitive capability, using an electric field parallel to the motion of the heavy ions.

The position measurement is accomplished as the ions enter the isobutane filled chamber, where they pass through a series of equipotential surfaces defined by a plane of thin horizontal and vertical wires that generate a uniform electric field that is parallel

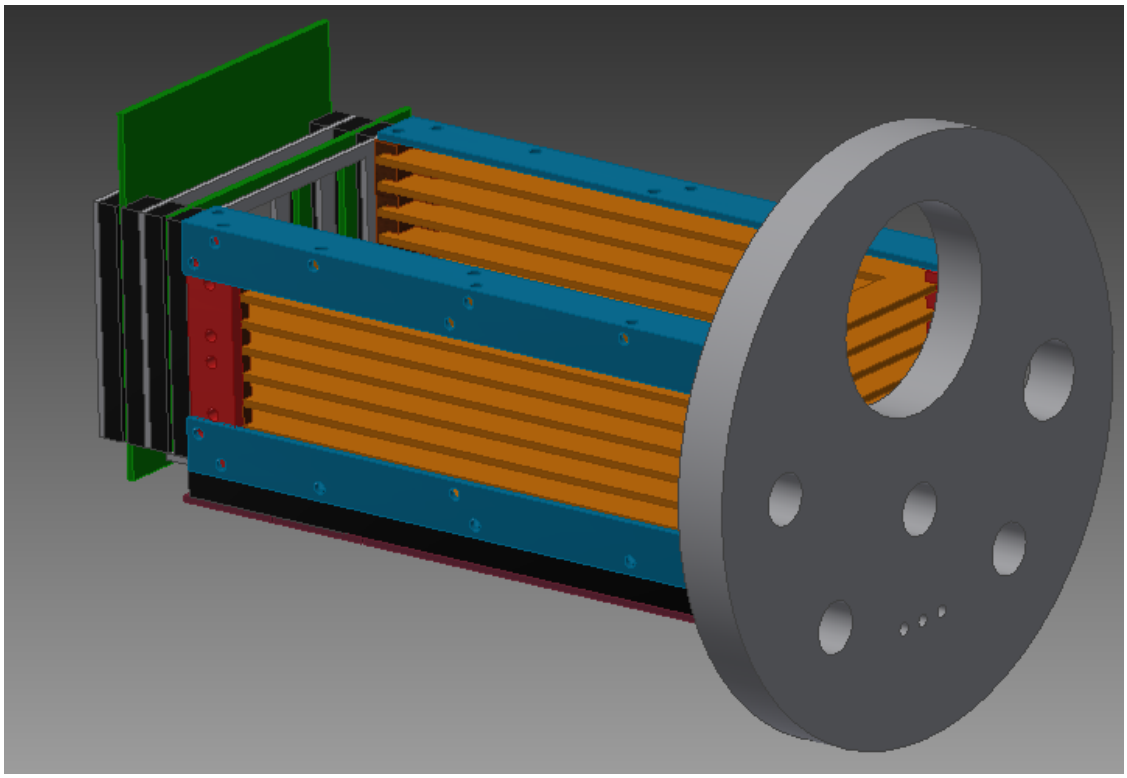

Figure 6-2: An isometric view of the 3D CAD model the ion chamber was constructed from.

to the direction of motion of the incident heavy ions. These wires are suspended by frames or printed circuit boards (colored green in the CAD model Fig. 6-2). There are five parallel frames in total arranged as alternating ground (cathode) planes and positively-biased anode planes. These thin gold-plated tungsten wires, of 25 µm diameter, are equally spaced over the frame and can be seen looking down the beam axis in Fig. 6-4. The wires are spaced 2 mm apart from one another in the grounded grids while the position-sensitive grids have wires that are 3 mm apart to give a larger area (100 mm x 100 mm) with fewer signals for the position-sensitive grids.

As the incoming particles ionize the gas, electron-ion pairs are created according to the properties of the gas, as discussed previously for isobutane. The electrons are then accelerated toward, and collected on, the positive horizontal or vertical wires. The

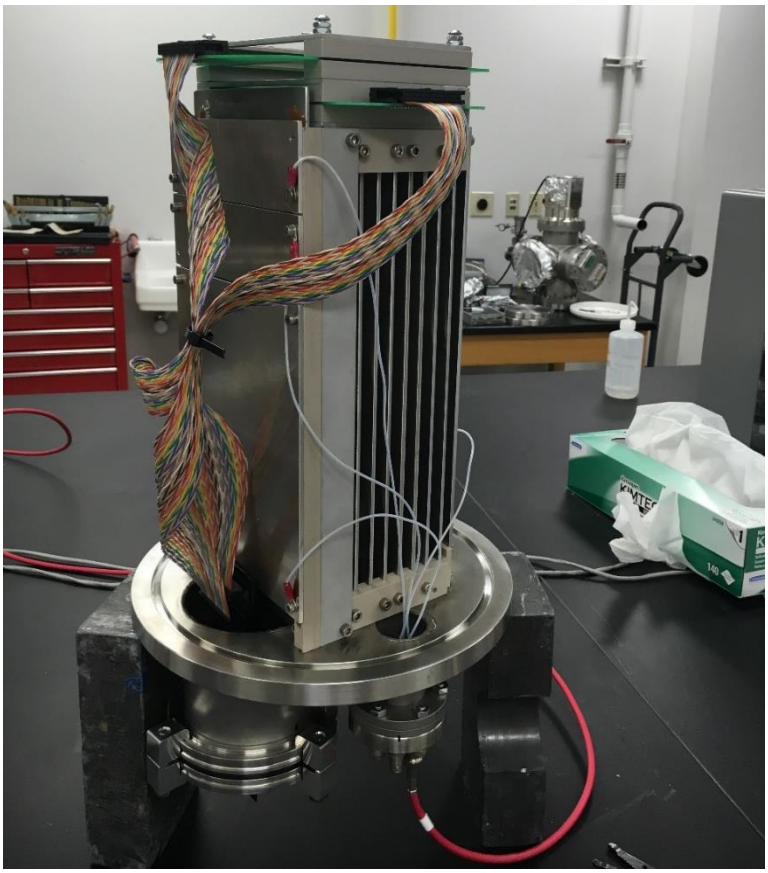

Figure 6-3: The ion chamber electronics being wired in the lab at LSU for testing.

signals induced on each wire are then read out separately and can be plotted as function of position with the net result being a x-y position measurement of the incoming particles with a resolution of 3 mm or less. This approach of position measurement has been used in counters developed by LSU for use at Florida State University (FSU), Michigan State University (MSU), and with the Helical Orbit Spectrometer (HELIOS) at Argonne National Laboratory [30]. While the wires do block some of the beam as it travels through the ion chamber, the loss of efficiency for these wires spaced 2 mm apart is less than 1% per grid giving total transmission of 94.7% [30].

Following the position measurement section of the ionization chamber is a section that uses a traditional approach with a uniform electric field perpendicular to the direction of the incident ions. This more traditional transverse geometry achieves better

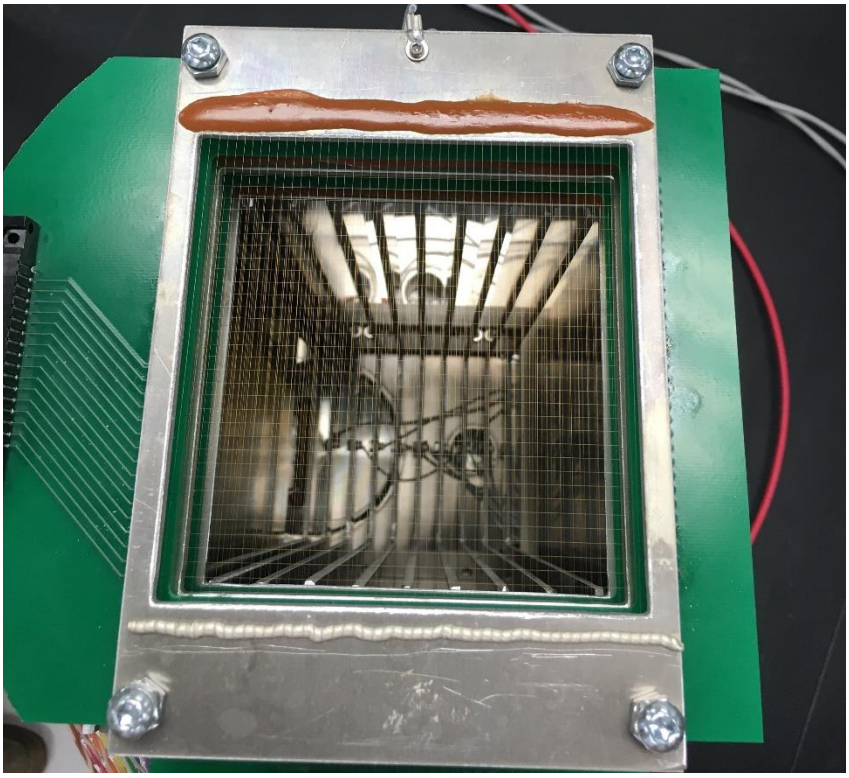

Figure 6-4: Looking down the beam axis of the ion chamber. The position-sensitive wires are seen at a 90-degree angle to each other.

energy resolution and eliminates wires in the path of the incident ions that reduce efficiency and introduces slight non-linearities into the energy measurement [30]. The transverse electric field is established by a set of uniformly spaced field-shaping electrodes that are held at regular voltage differences supplied by a voltage divider to create a uniform electric field. In total, there are 10 such field shaping electrodes utilizing the base of a 10-stage PMT tube as the voltage divider between them, as seen in Fig. 6-5 and Fig. 6-6. As the particles enter this section of the ionization chamber and ionize the isobutane, the electrons are swept towards three anode plates, while the positively charged heavy ions are swept in the opposite direction toward the cathode plate. The upstream part of the chamber has two smaller anodes, 5 cm in length each, for two ΔE measurements followed by a longer 20 cm anode for residual full energy

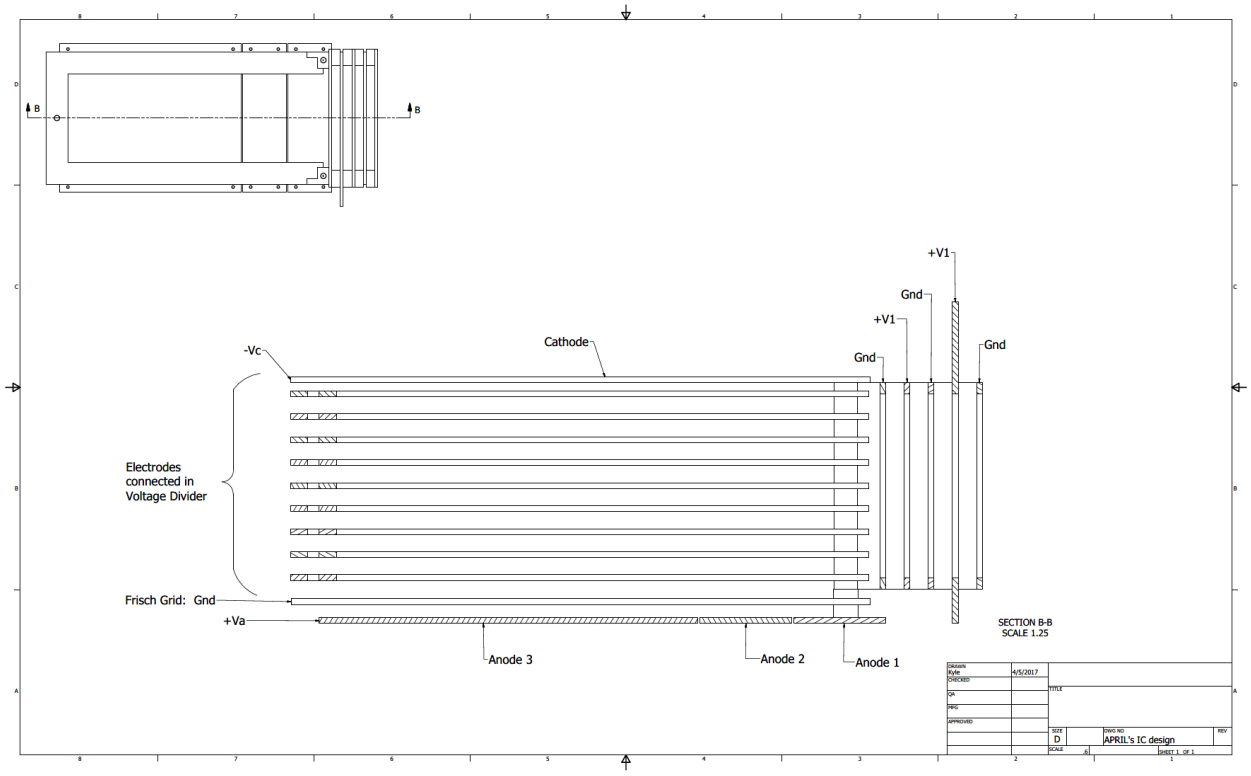

Figure 6-5: Side-section view of gas ionization chamber, with ions entering the chamber from the right. The electronics shown indicate where the potentials lie on the electrodes in both the position-sensitivity and energy measurement sections. Typical voltages are 8 V Torr^{-1} in the anode (Va) and 4 V Torr^{-1} in the cathode (Vc) [28].

measurement. The current collected on each anode relates to the amount of energy lost from the ionization of the incident particle in that section. The higher Z ions traveling through the gas lose more energy to ionization in the first two anodes (compared to a lower Z ion) for the same total energy-loss. This ΔE-E technique provides the necessary information for Z discrimination of the heavy ion. This discrimination is more effective for lower Z [2]. A plot of the energy-loss versus total energy was shown in Fig. 6-1 for an experiment using this type of ionization chamber to separate the ^{18}F recoils from the ^{17}O beam.

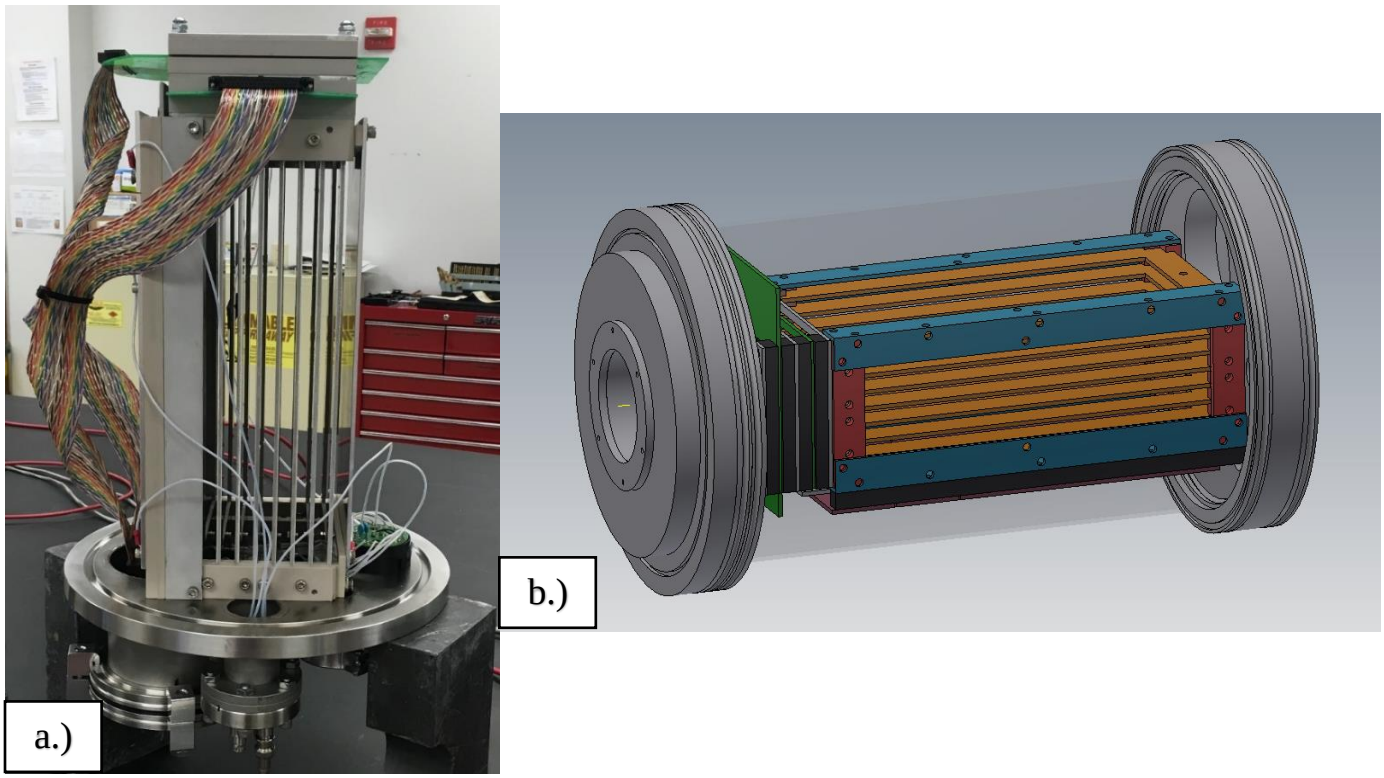

Figure 6-6: a.) Side view of ion chamber wired to outputs in lab. The uniformly spaced field-shaping electrodes plates are connected in a voltage divider and supply a uniform electric field. b.) Electronics of ionization chamber inside cylindrical housing (transparent here) that will contain isobutane gas.

An important feature of the design is a grid of grounded wires placed in front of the anodes to shield them from induced potential from the electrons as they travel towards the anodes. If this shielding, known as a Frisch grid, is not present, the induced potential reduces the timing resolution of the signal as the signal and results in a response that is dependent on the position of the leaving ion and initial ionization [31].

One limitation of this type of ionization chamber design arises from the heavy ions that are slow to move in the electric field. One heavy ion may not make it to the cathode before the second enters the counter, restricting the overall flux of incoming beam as to not produce pileup. However, with the modest radioactive beam intensity and excellent rejection of SECAR, the count rate at the focal plane is sufficiently low

that pileup should not be an issue for the ionization chamber. The chamber of a similar design operated at rates of more than 10^4 particles per second without significant pile up [32].

The ionization chamber can be removed from its housing for maintenance as shown in Fig. 6-7. Also, for measurements at low energies, the entire ion chamber (including the chamber) can be retracted for substitution of a silicon strip detector which provides better total energy resolution than the gas ionization detector at the same energy. The silicon strip detector also does not require a gas chamber which eliminates energy-loss of the ions by the ionization chamber window. For this purpose, we plan to use a standard off-the-shelf double-sided silicon strip detector design from Micron Semiconductor, shown in Fig. 6-8. The detector will be repackaged onto a printed circuit board (PCB) that has a smaller footprint that may allow the silicon

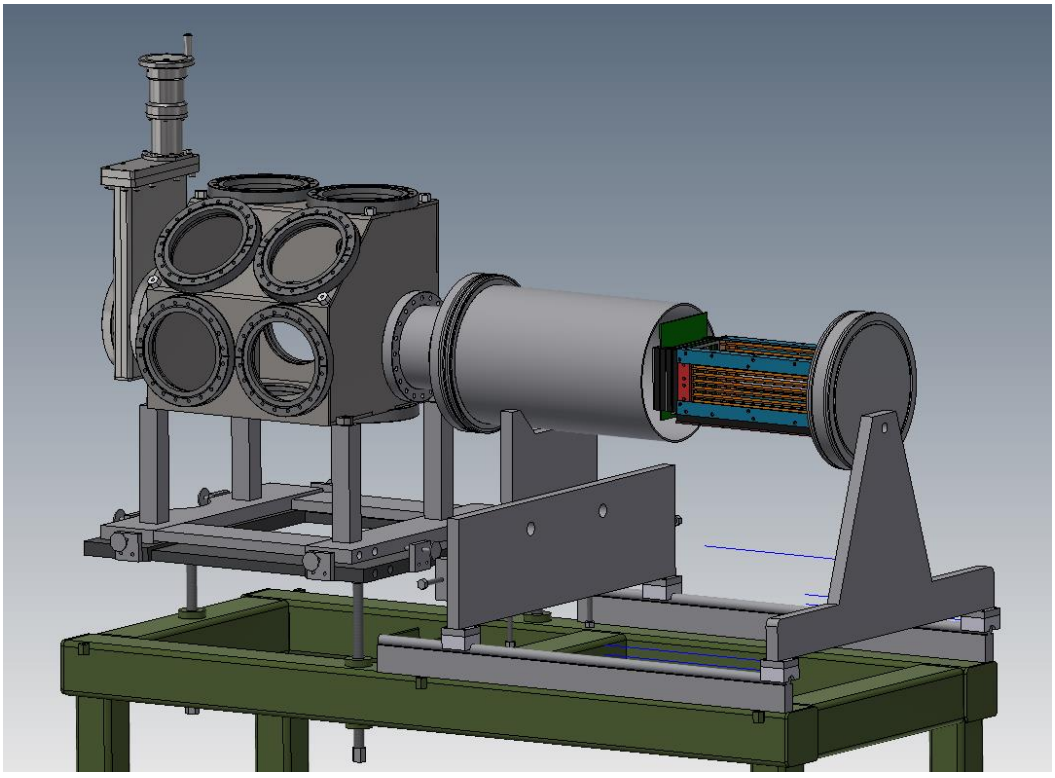

Figure 6-7: Electronics of ionization chamber in exploded view showing the removability from the housing.

to be used in the future as a stopping detector inside the ionization detector. The design BB-7 detector has 32 strips on each face with 2 mm pitch, for a full active area of 64 mm x 64 mm. This is smaller than the acceptance of the ionization chamber, but this size should be sufficient since the silicon detector will be located close to the ion-optical focus using a new compact chamber designed especially for this purpose.

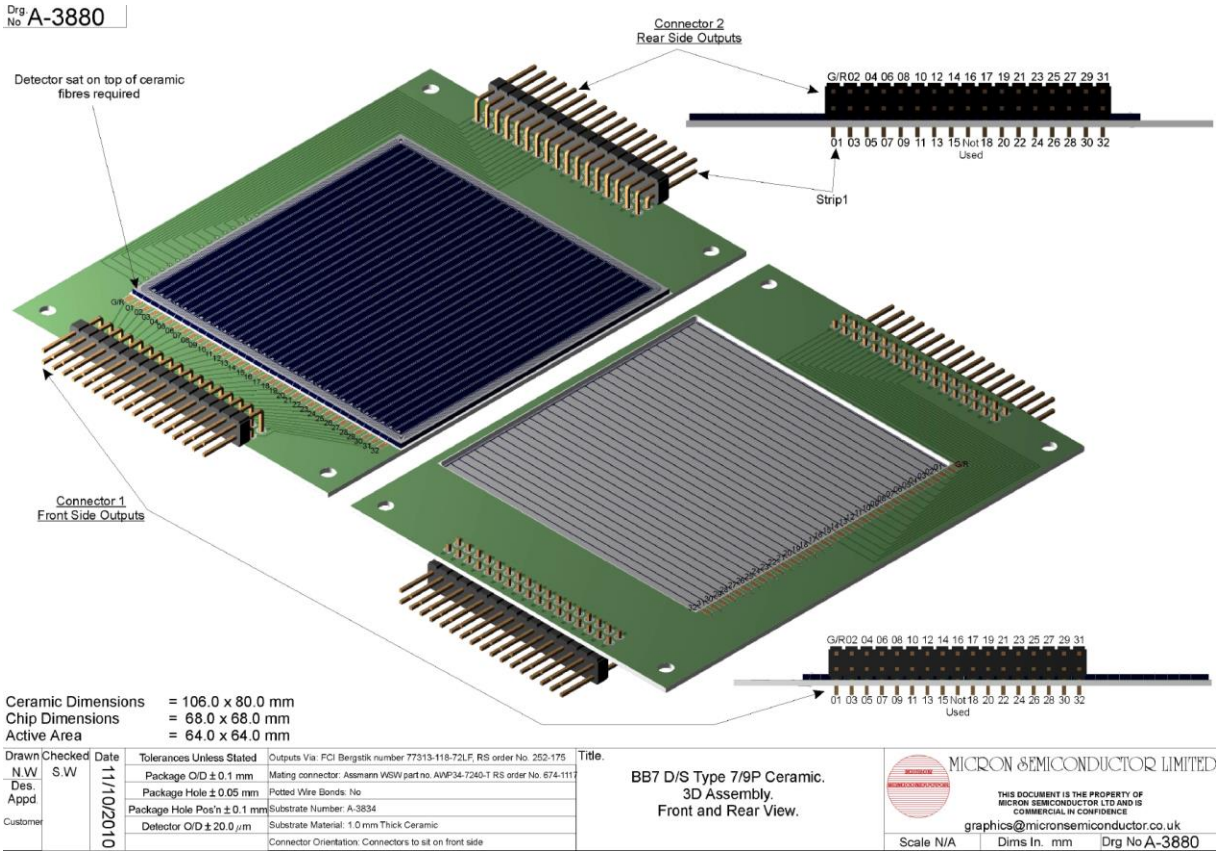

Figure 6-8: Double-sided silicon strip detector design from Micron Semiconductor that will be used as a stopping detector in substitution of the ion chamber. The detector package will be a printed circuit board that is being designed to reduce the overall package size.

CHAPTER 7. CONCLUSIONS

7.1. Final Remarks

The exciting new physics possible with SECAR will answer questions regarding the nature of stellar thermonuclear explosions such as X-ray bursts and classical novae. SECAR will measure (p,γ) and (α,γ) capture reactions in inverse kinematic process where the heavy reaction products are measured after being separated from the overwhelming number of unreacted beam particles. SECAR is being installed in the ReA3 hall and will concentrate on the energy range of 0.3 MeV/A to 3 MeV/A and the mass range of $A = 15 - 65$, matched to the most important energies for stellar explosions. The resonance strength sensitivity is at least 100 meV, down to possibly better than 1μeV for the best case. SECAR's technical aspects include a total particle rejection of order 10^{-17}, an angular acceptance of ± 25 mrad, and an energy acceptance of ± 3.1%. Discrimination of the recoils is possible through a separator of mass resolution of ~750 and a factor of 10^{-4} discrimination by the detector systems.

The focal plane for SECAR is designed to accommodate a variety of instrumentation including two micro-channel plate detectors and a gas ionization chamber. The MCPs provide precise position and time-of-flight measurements while the ionization chamber measures the total energy of the ions and discriminates atomic number *(Z)* via relative energy-loss. Time-of-flight measurements using the MCP detectors are more effective for separating relatively slower and heavier low-energy recoils whereas gas ionization is more selective for faster and lighter ions. The time-of-flight measurement from the MCP and the energy-loss measurement from the ionization chamber provide an excellent initial set of parameters for discriminating the heavy ion recoils from the unreacted beam at the SECAR focal plane. Additionally, the configuration of these detectors at the focal plane allows for other instrumentation such

as silicon strip detectors or scintillators used in place of a gas ionization chamber for total energy measurements, which could be advantageous especially in the lower energy regime [2].

The chambers, stands, and horizontal adjustment plates were designed in Autodesk Inventor with the goal of creating a flexible configuration for the experiments in SECAR. The properties of beams available in the future may present the need for additional detectors to be placed in the focal plane chambers, and the easy addition or substitution of new parts in the design will allow for quick and simple modification of SECAR for many future experiments.

7.2. Timeline Of Events

The gas ionization detector will be tested at FSU with beams from the LINAC. The focal plane stands, adjustable plates, and chambers are currently being constructed at LSU. The timing and position resolution of the MCPs will be tested at LSU using alpha sources in the summer and fall of 2017. The focal plane will be delivered to MSU before the end of 2017, with installation occurring in time for possible commissioning in late 2018. FRIB is scheduled to be completed in June 2022 and is managing to early completion by December 2020 [33]. The SECAR project is also managing to an early completion in April 2020, and will be available for the first experiments at FRIB.

APPENDIX: TECHNCAL DRAWINGS

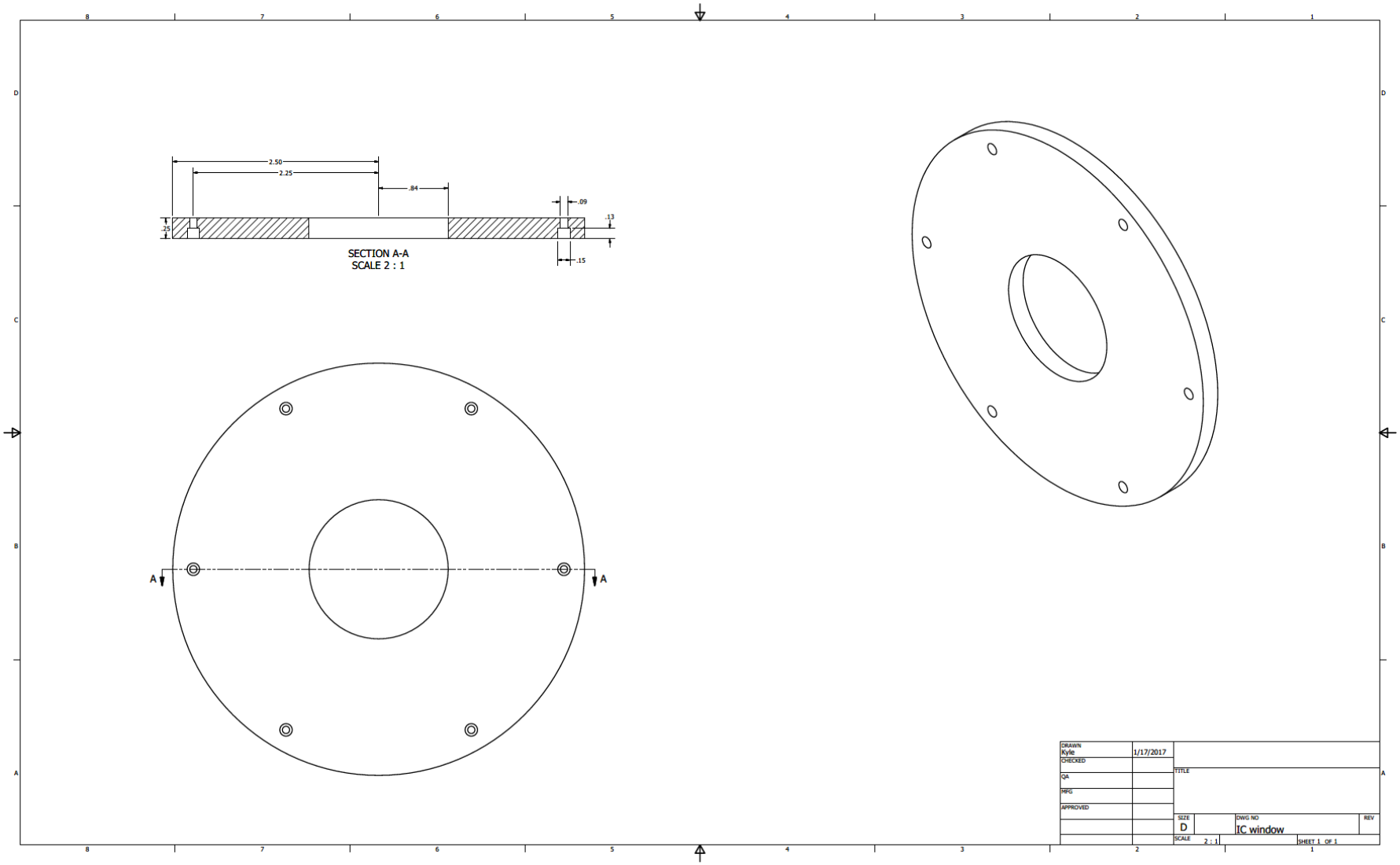

Figure A-1: Ion chamber window.

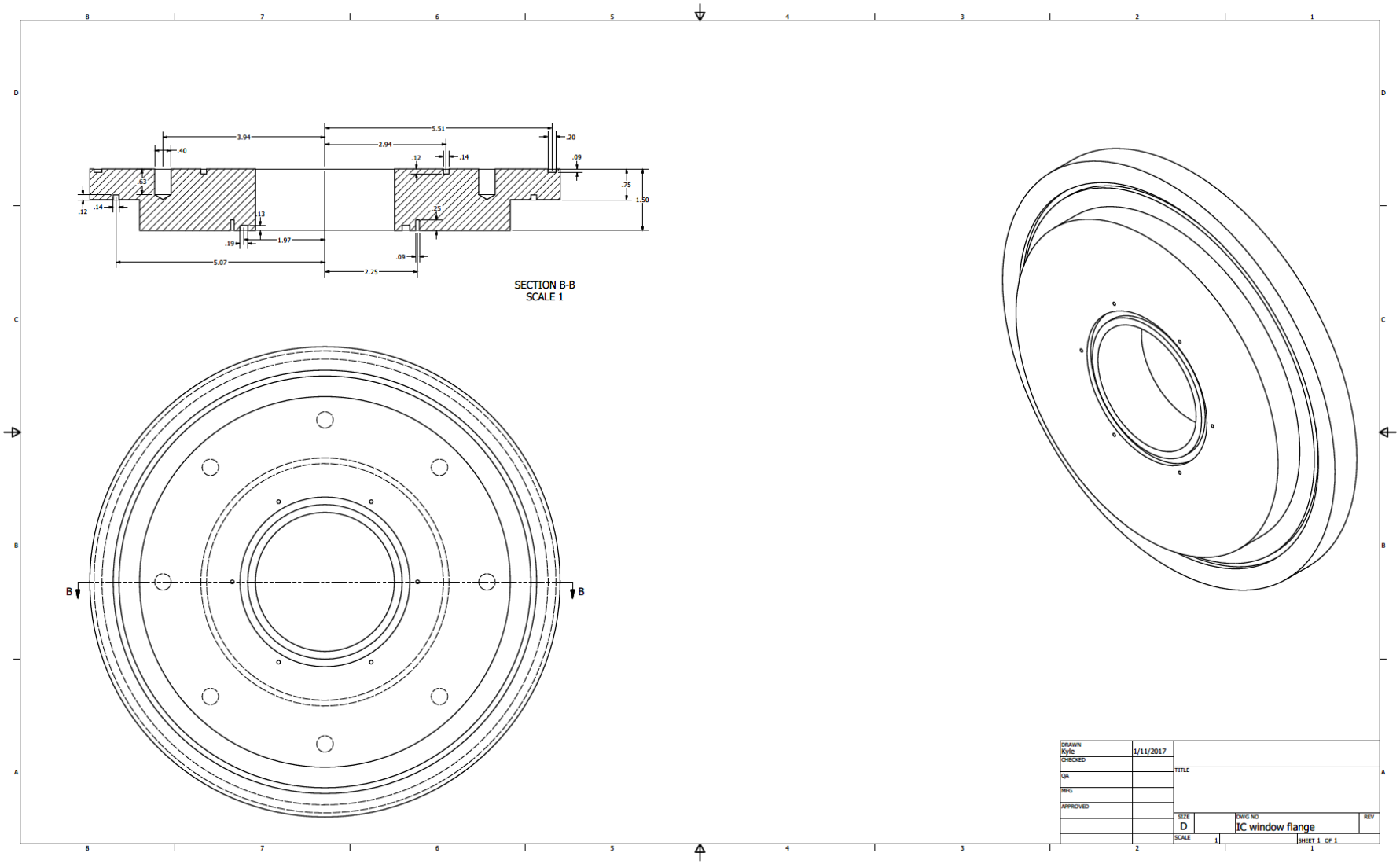

Figure A-2: Ion chamber window flange. Smaller diameter side will face downstream.

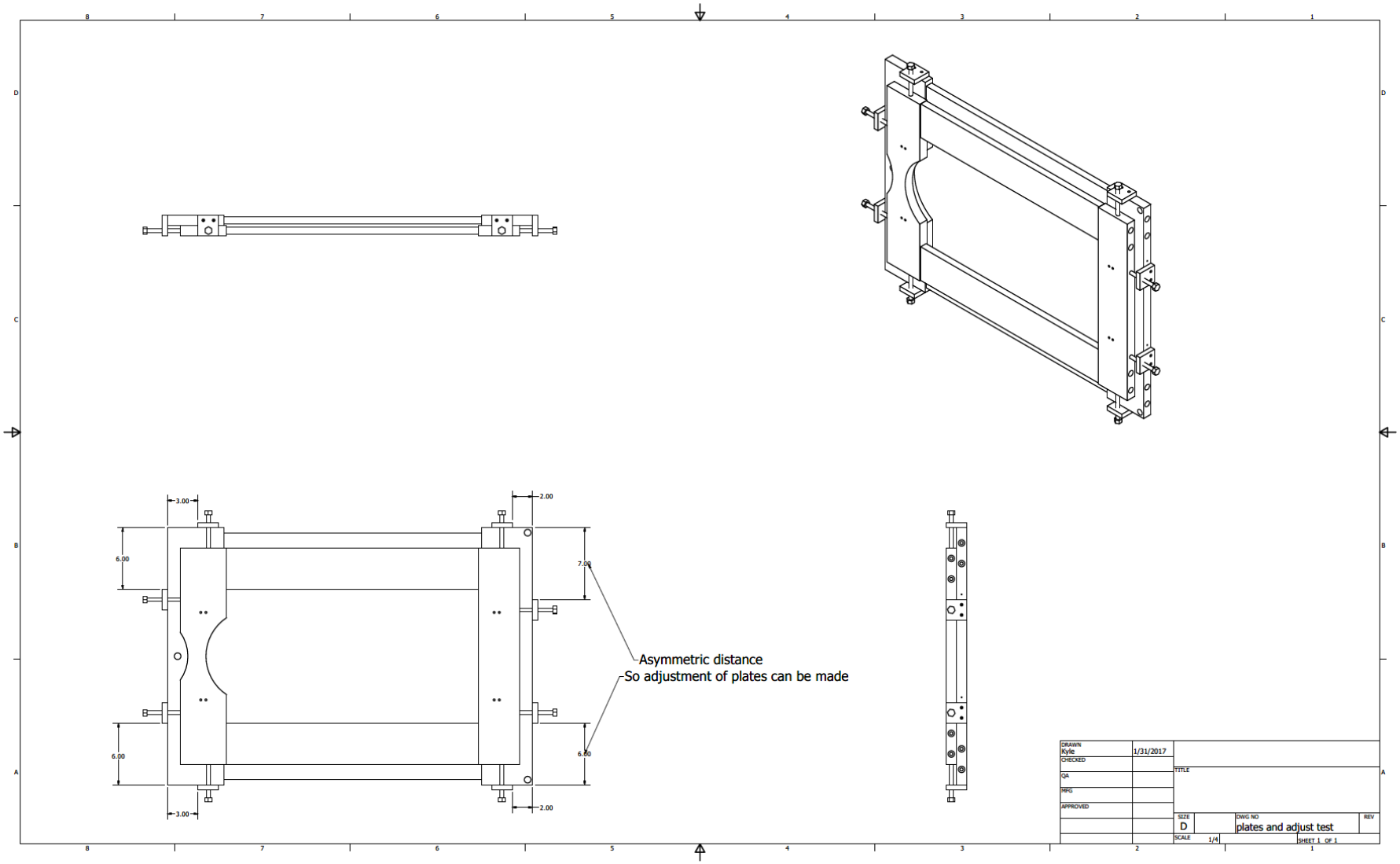

Figure A-3: Drawing of adjustable plate assembly for relative dimensions.

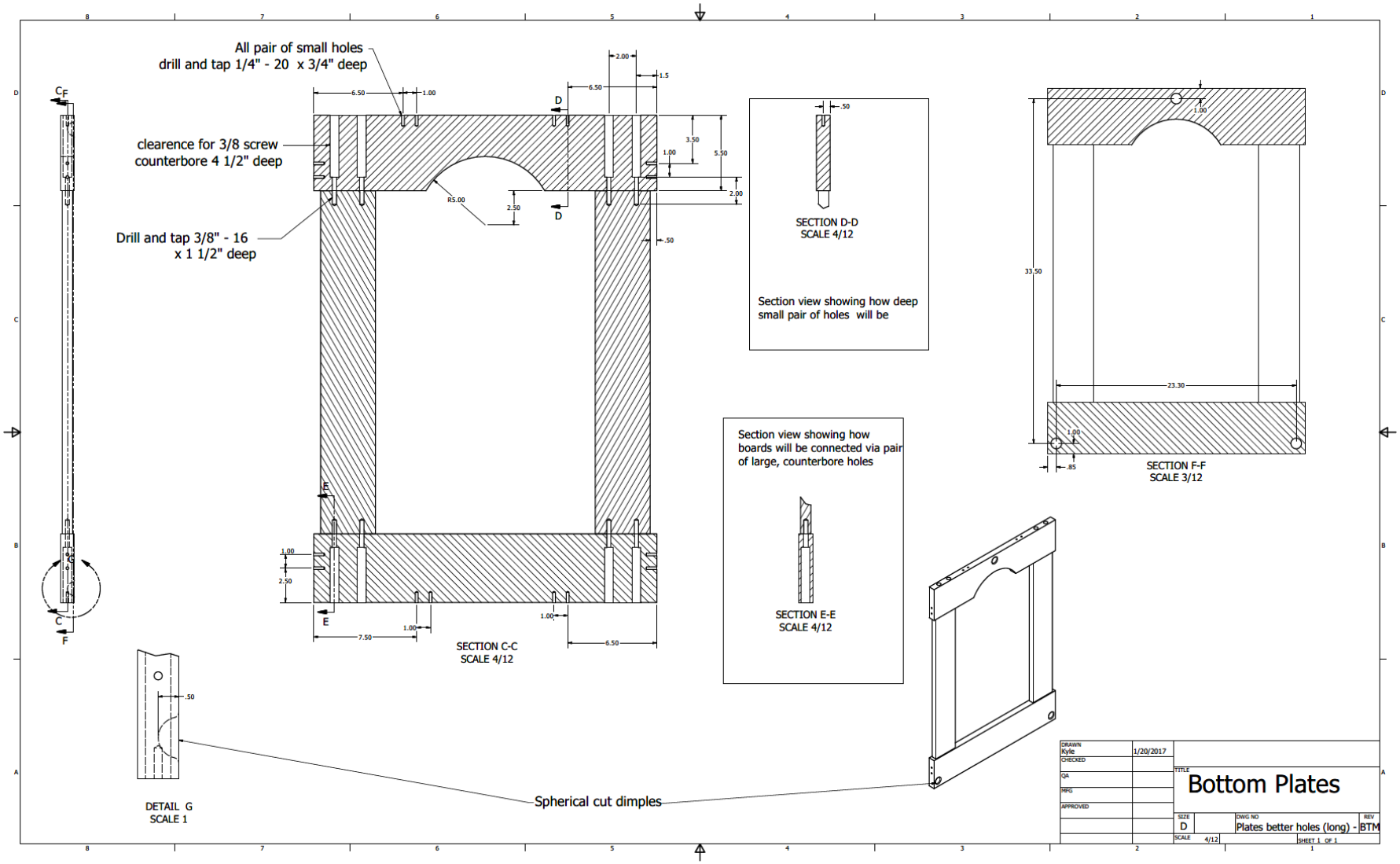

Figure A-4: Technical drawing of lower (bottom) adjustable aluminum plates.

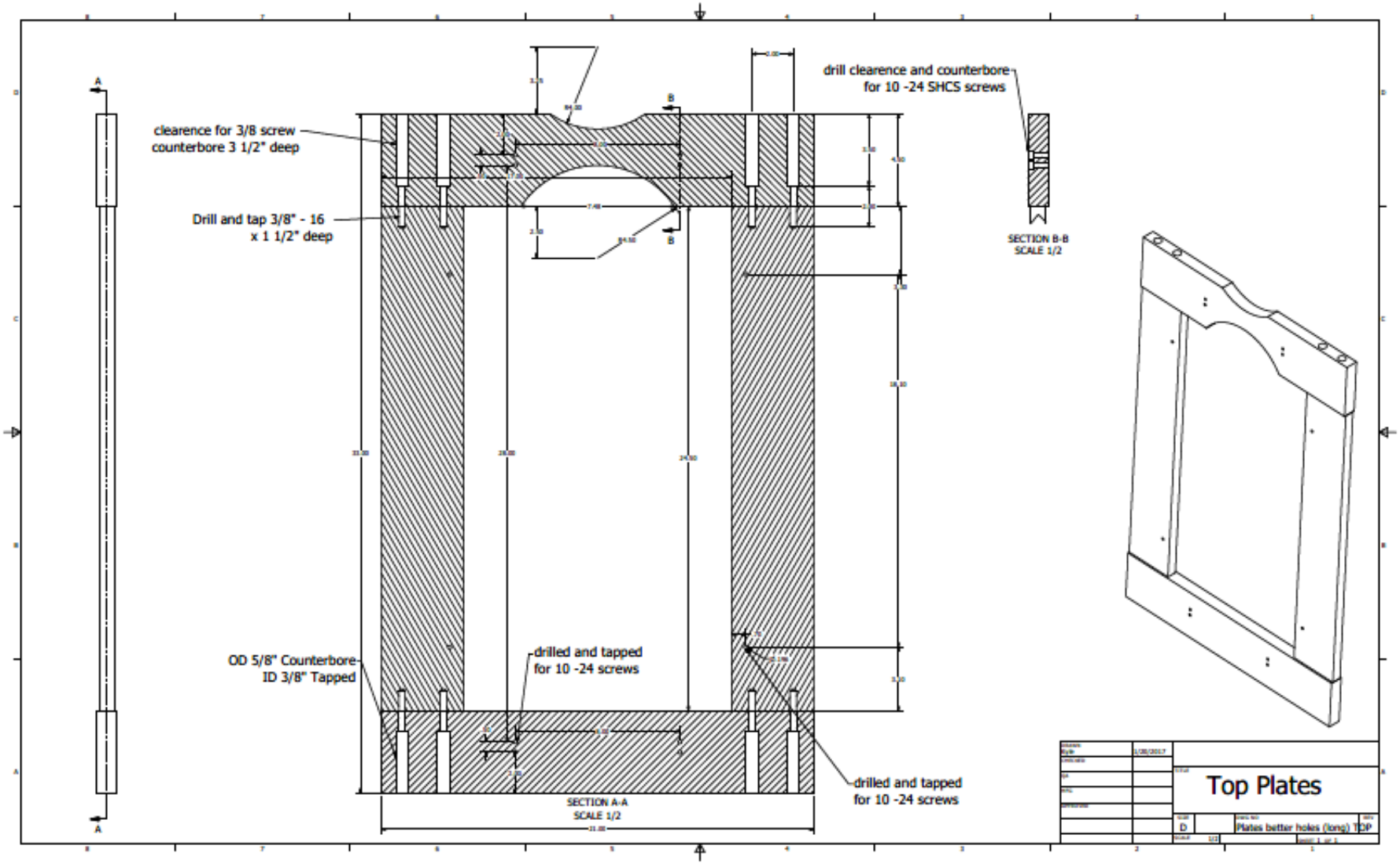

Figure A-5: Technical drawing of upper (top) aluminum plates.

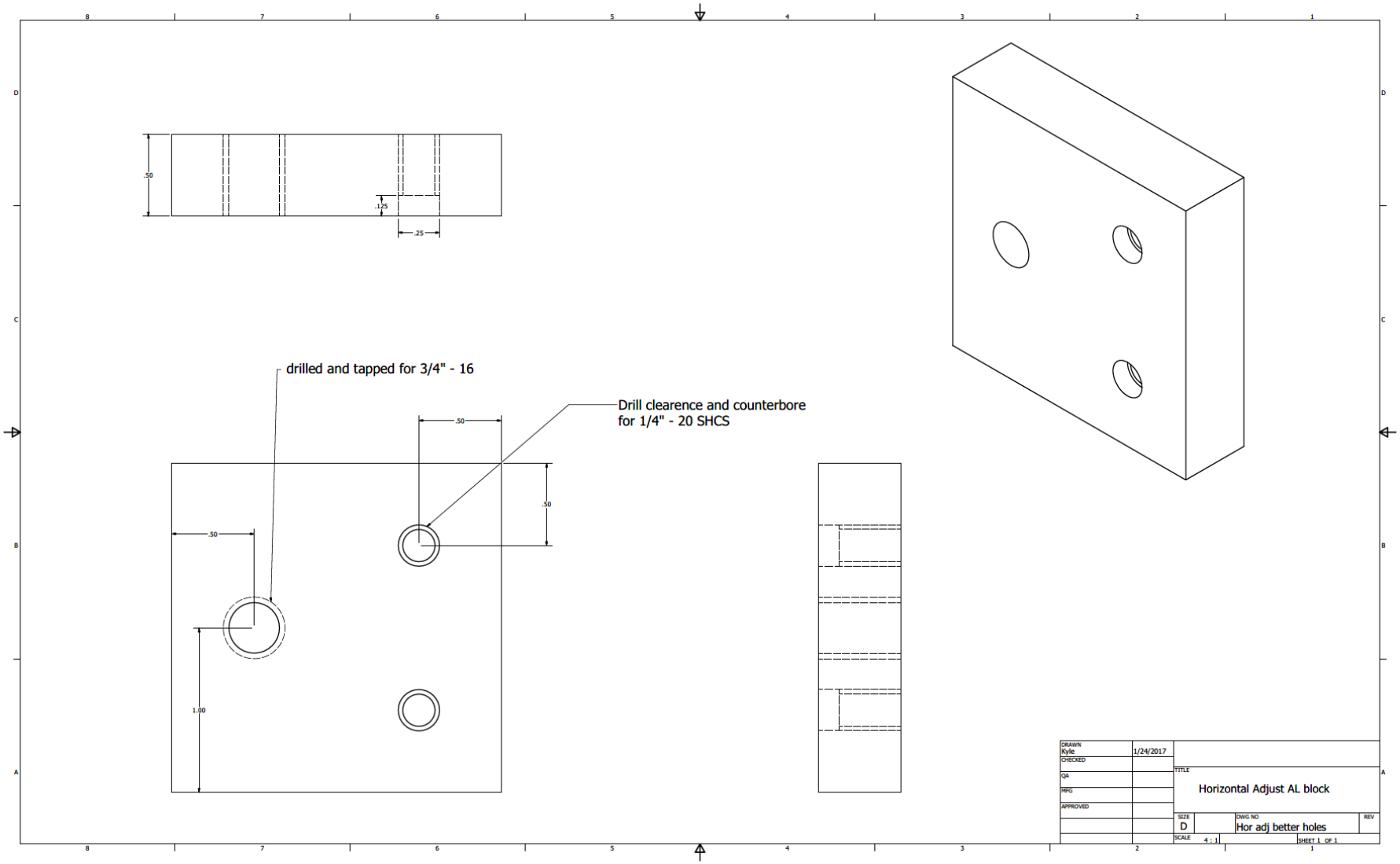

Figure A-6: Technical drawing of adjustable aluminum blocks that hold the jack screws for the adjustable plates.

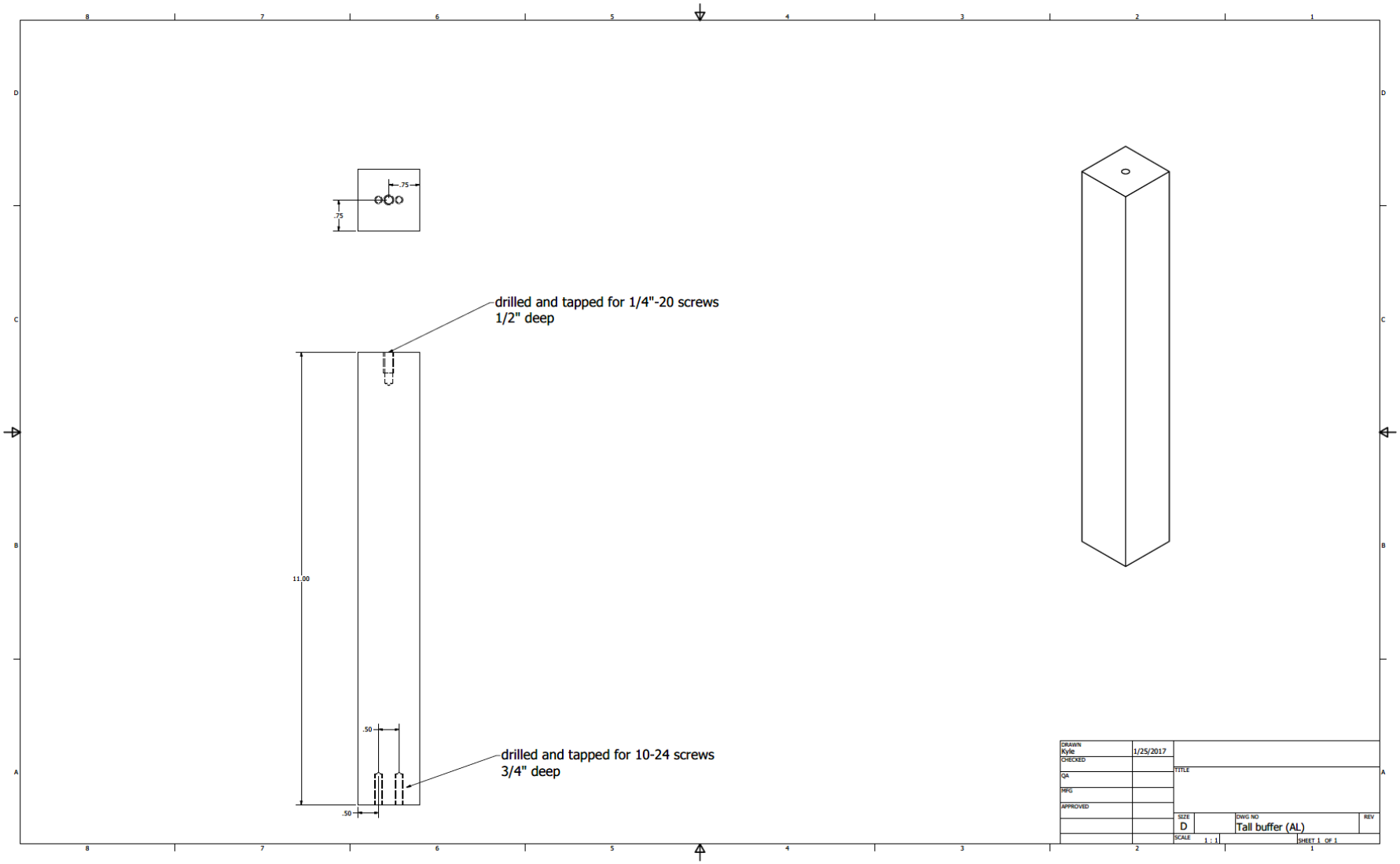

Figure A-7: Aluminum pillar. Bottom (2 holes) connects to adjustable plates. Top (1 hole) connects to steel tab.

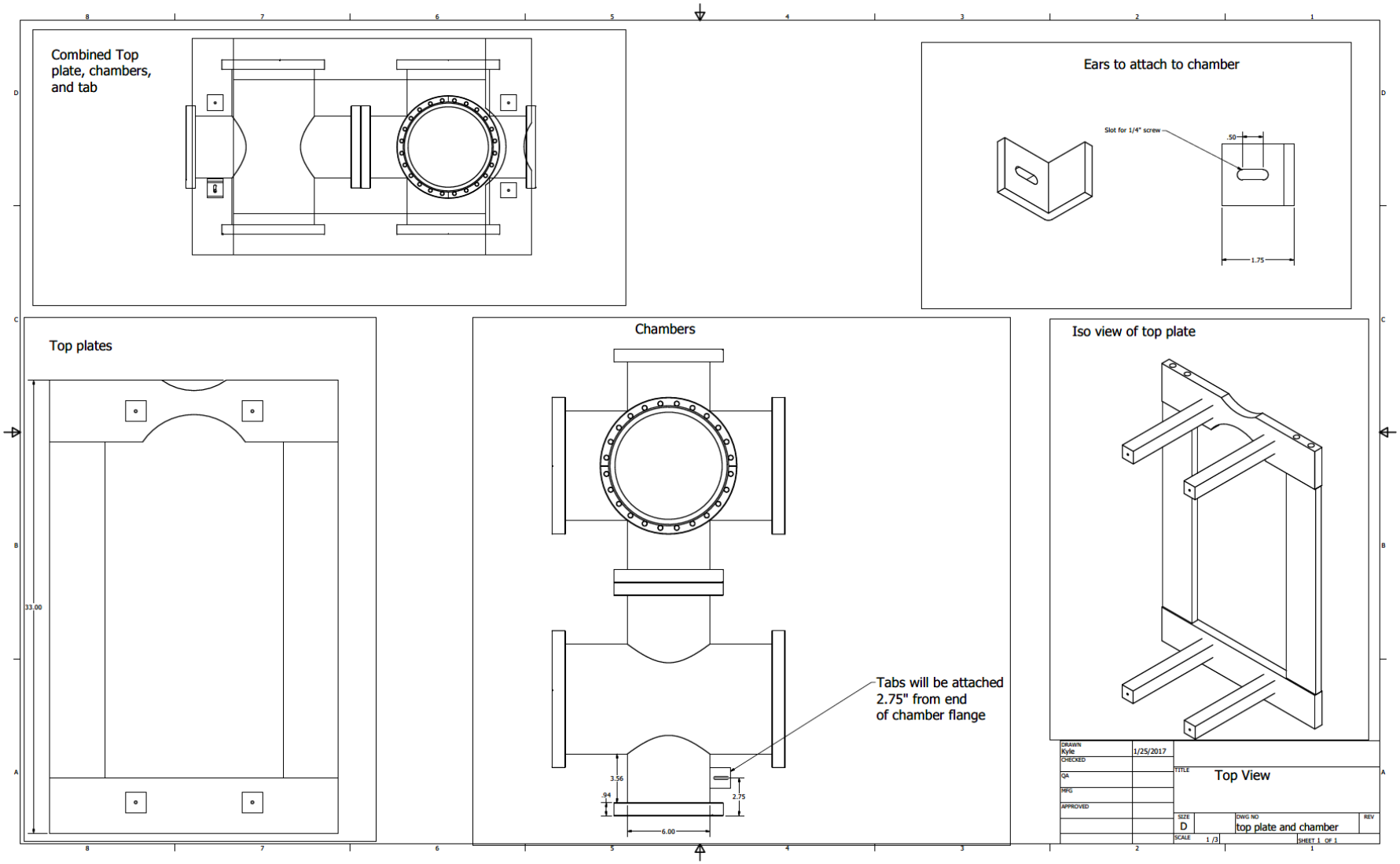

Figure A-8: Drawing showing the connections from the adjustable plates, to the aluminum pillars, to the steel tabs, to the chambers.

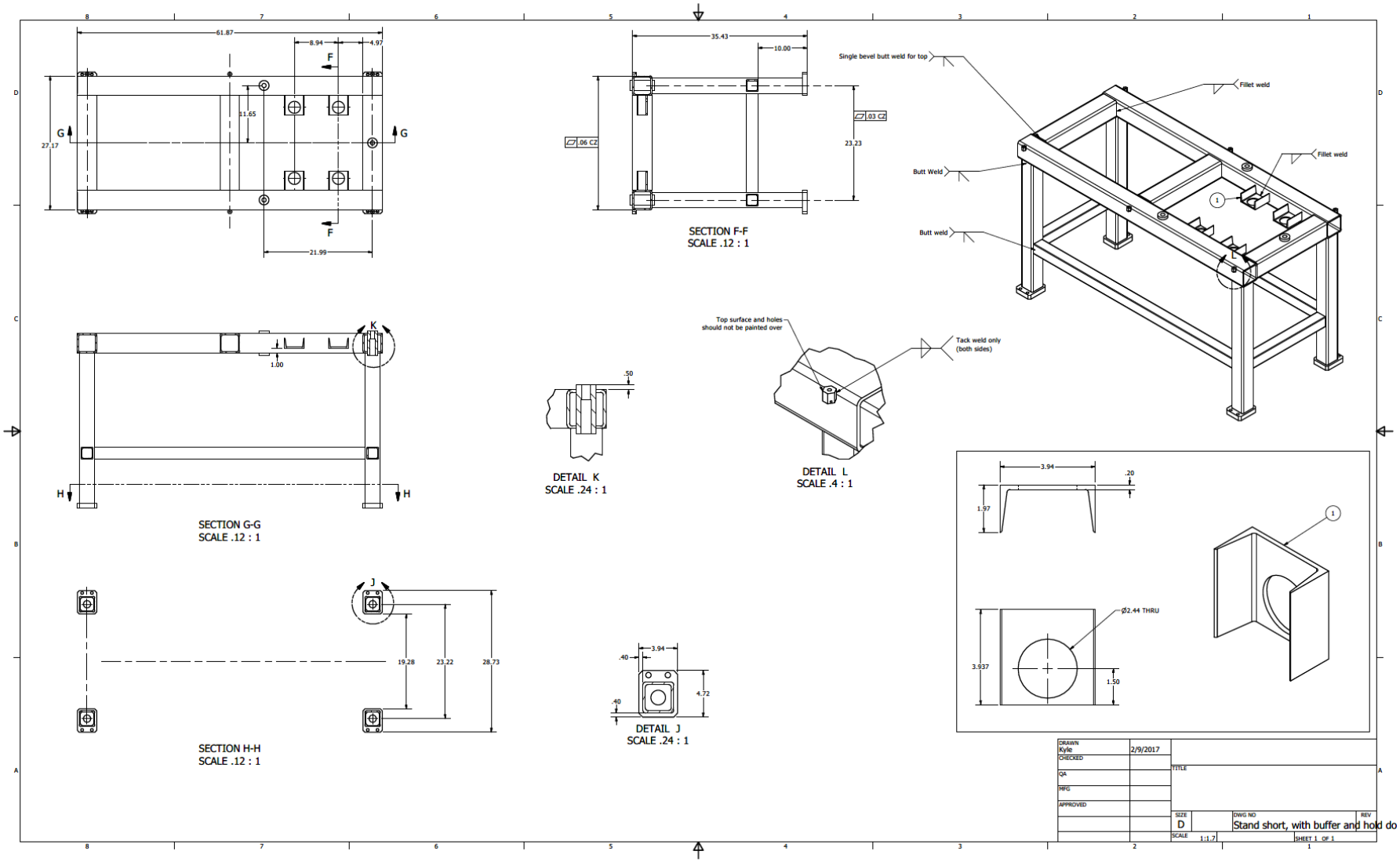

Figure A-9: Drawing of short steel stand including the tie-down tabs on the inside of the stand.

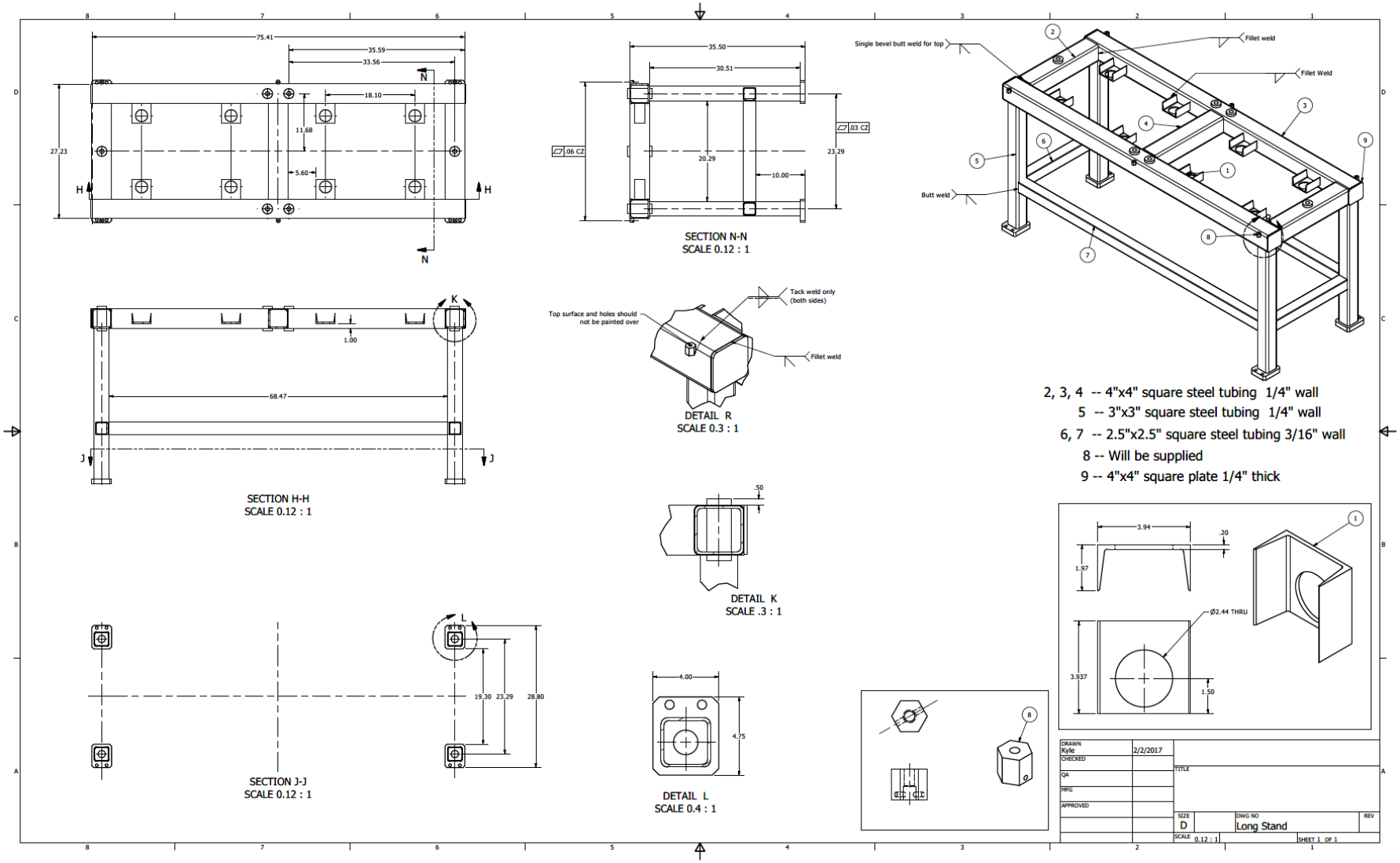

Figure A-10: Drawing of long steel stand including tie-down tables on the inside of the stand.

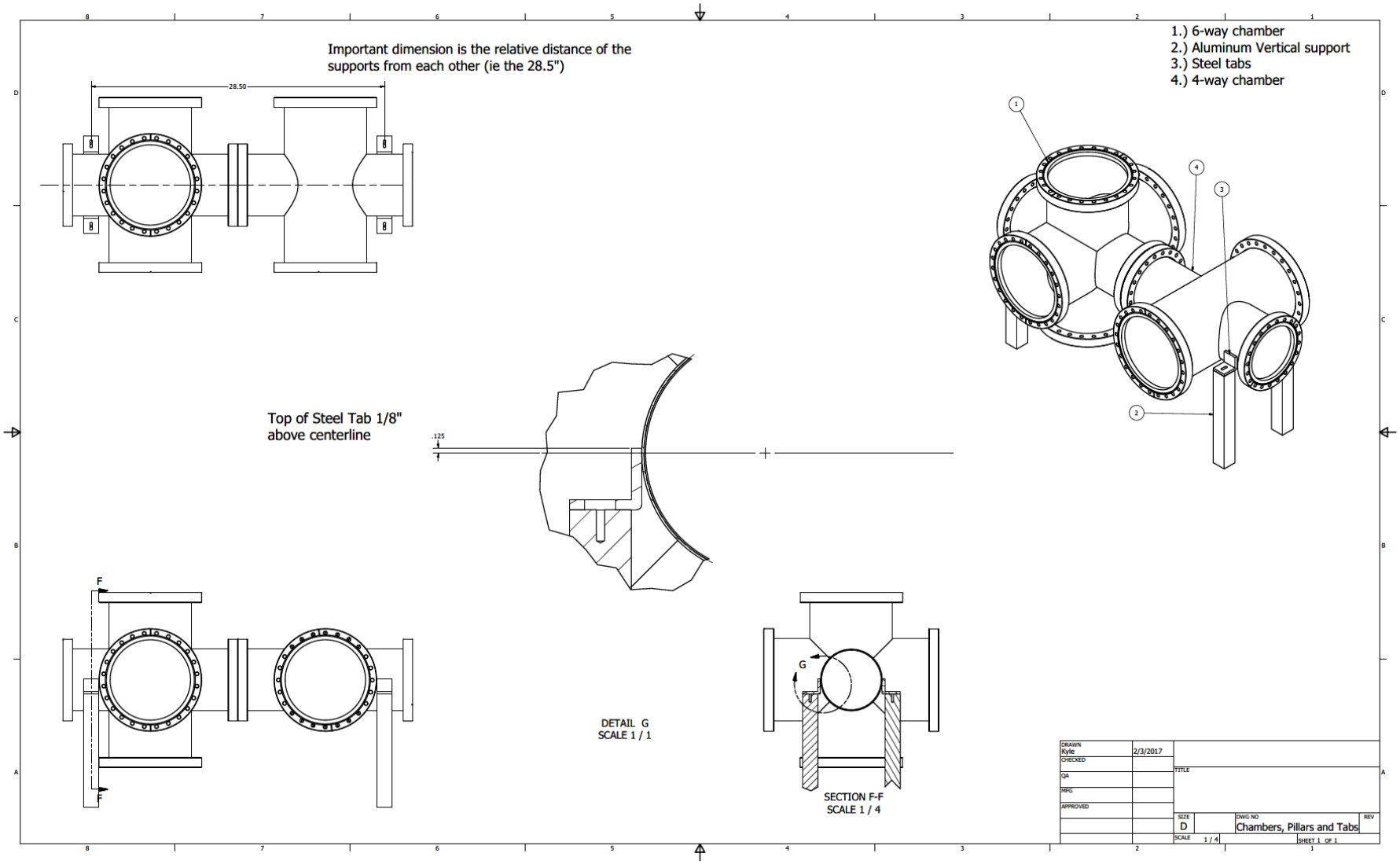

Figure A-11: Connection and alignment of steel tabs onto chambers.

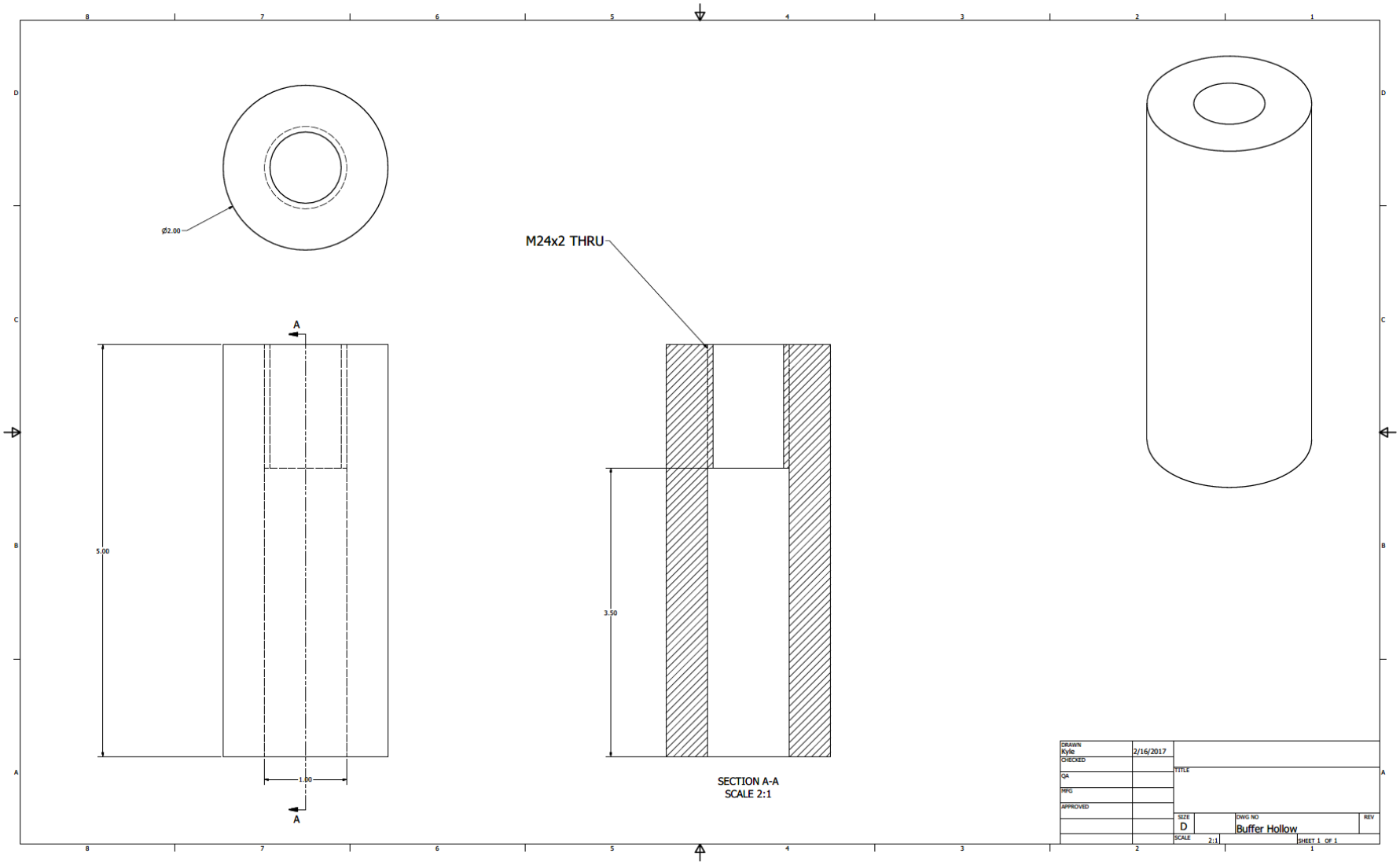

Figure A-12: Tapped steel inserts that hold vertical adjustment threaded steel rod.

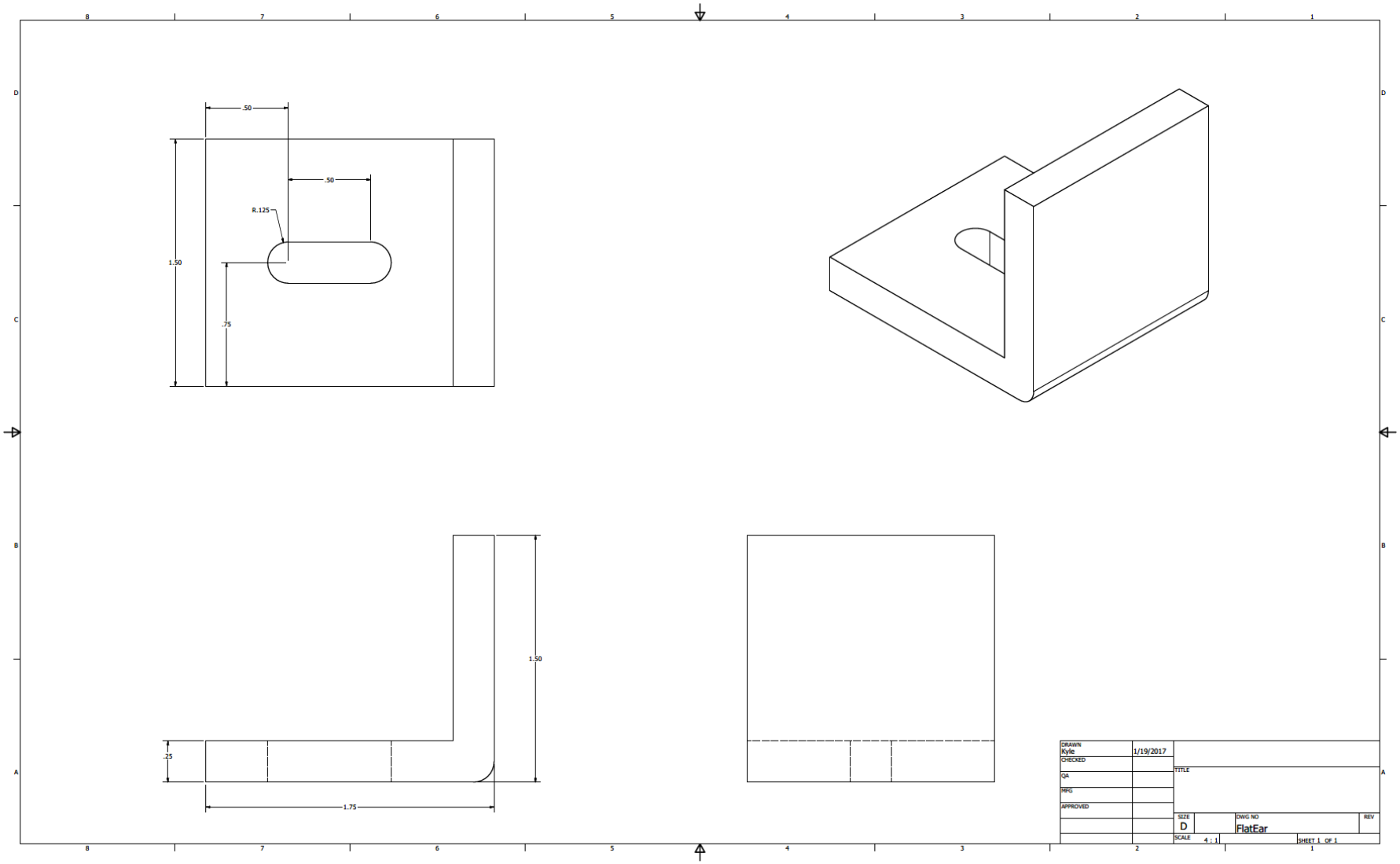

Figure A-13: Steel tabs that are welded to chamber and connect to pillar.

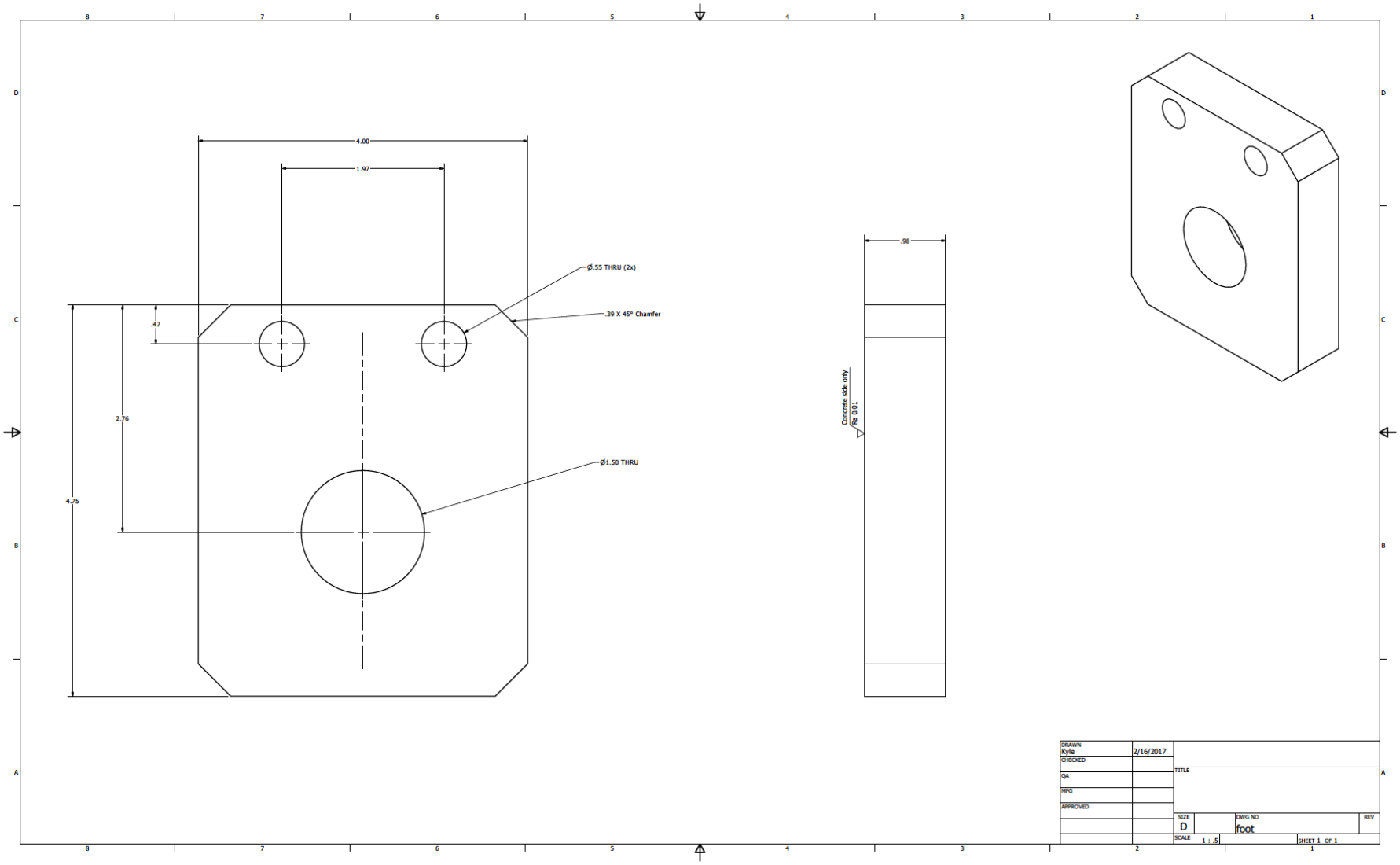

Figure A-14: Foot of both short and long steel stands that will connect to floor.

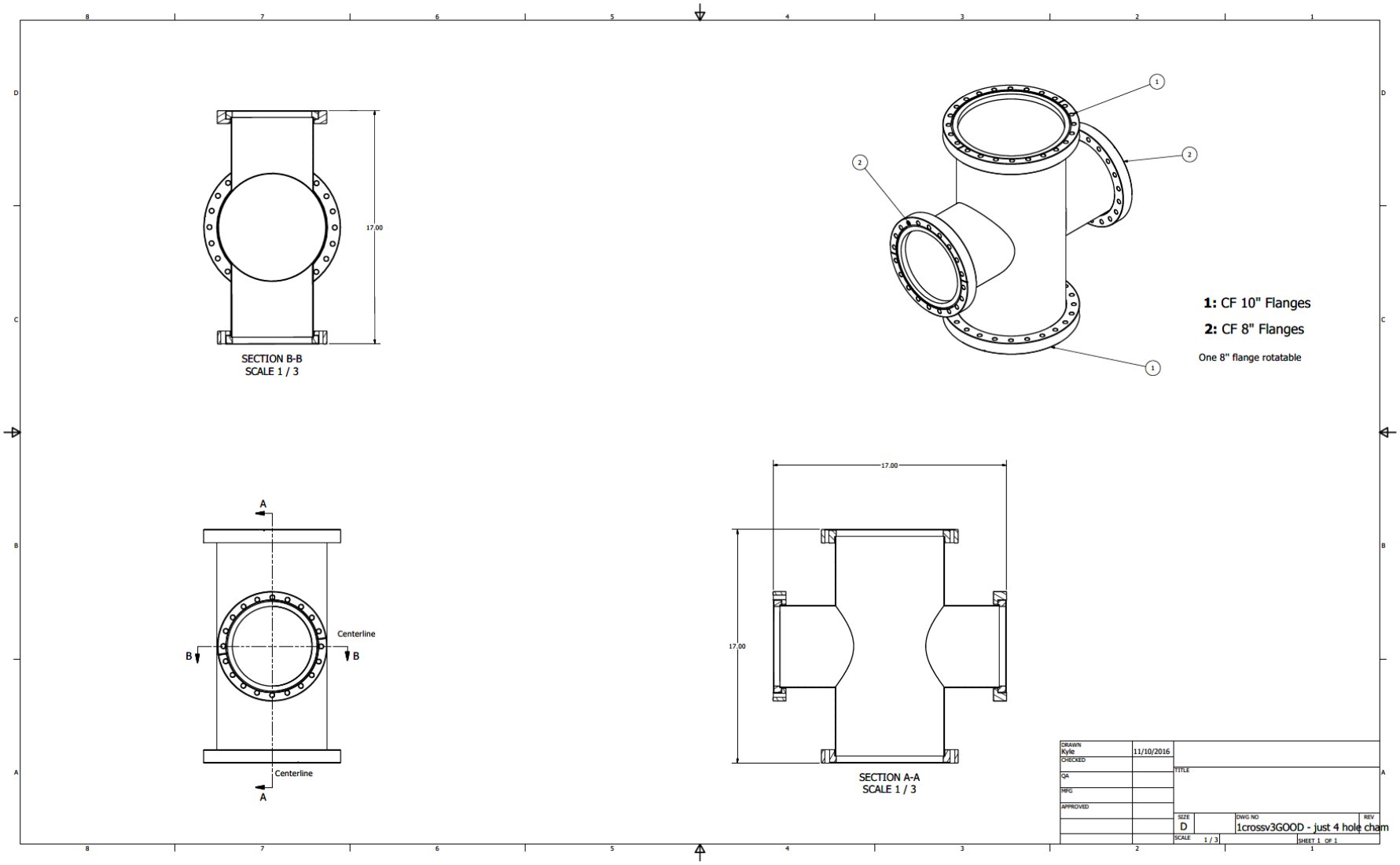

Figure A-15: 4-port chamber dimensions and flanges.

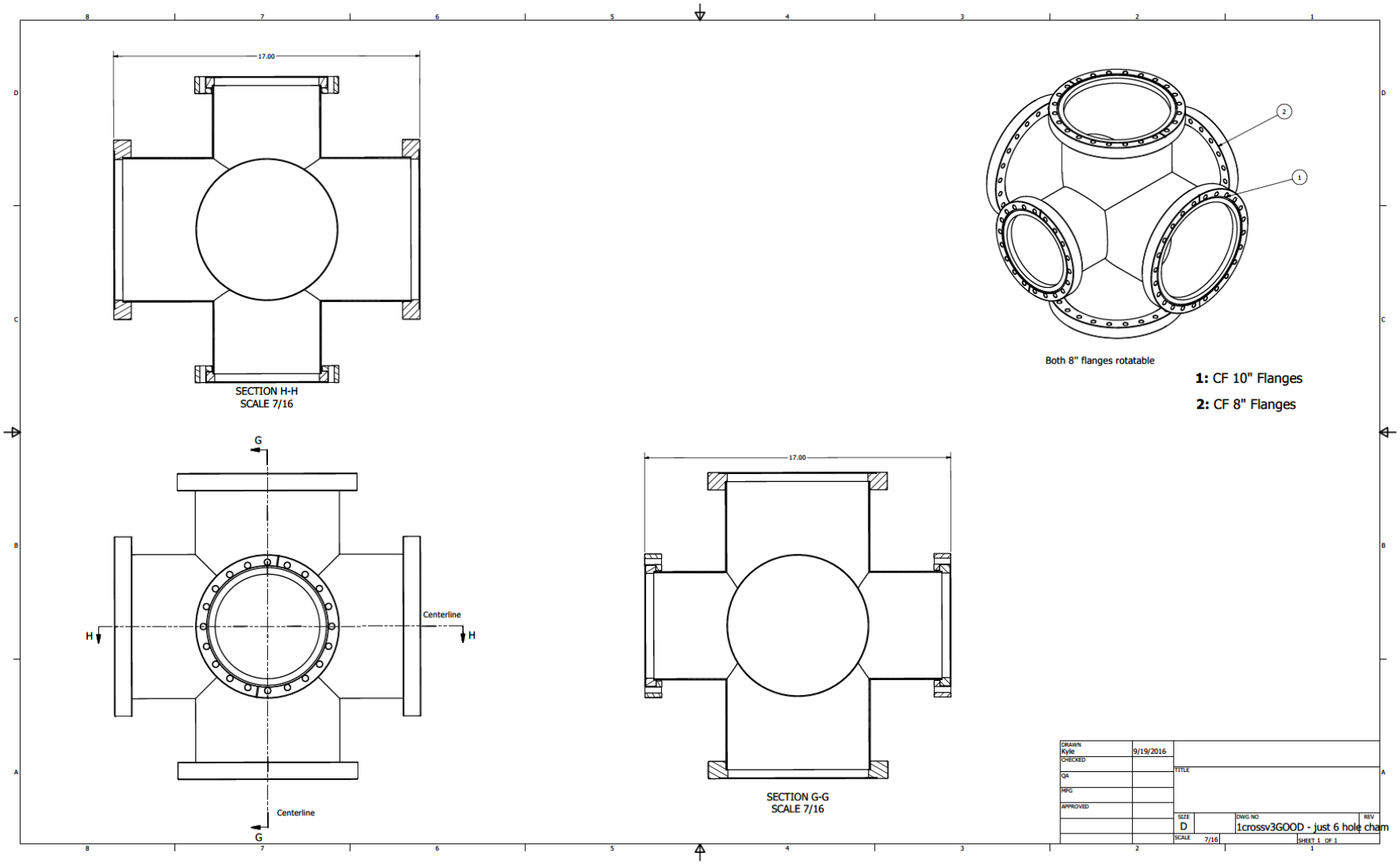

Figure A-16: 6-port chamber dimensions and flanges.

REFERENCES

[1] K. A. Chipps, U. Greife, D. Bardayan, J. Blackmon, A. Kontos, L. Linhardt, M. Matos, S. Pain, S. Pittman, A. Sachs, et al., Nuclear Instruments and Methods in Physics Research Section A: Accelerators, Spectrometers, Detectors and Associated Equipment **763**, 553 (2014).

[2] K. Rehm, A. Spyrou, M. Syphers, M. Wiescher, W. Wittmer, C. Wrede, X. Wu, and A. Zeller (2014).

[3] C. Iliadis, A. Champagne, J. José, S. Starrfield, and P. Tupper, The astrophysical Journal supplement series **142**, 105 (2002).

[4] Smith M. SECAR Collaboration Meeting. In: SECAR Science. East Lansing, Michigan: (2015).

[5] C. J. Hansen, S. D. Kawaler, and D. Arnett*, Stellar interiors: Physical principles, structure and evolution* (1995).

[6] C. Fröhlich, P. Hauser, M. Liebendörfer, G. Martínez-Pinedo, F.-K. Thielemann, E. Bravo, N. T. Zinner, W. Hix, K. Langanke, A. Mezzacappa, et al., The Astrophysical Journal **637**, 415 (2006).

[7] G. Magkotsios, F. X. Timmes, A. L. Hungerford, C. L. Fryer, P. A. Young, and M. Wiescher, The Astrophysical Journal Supplement Series **191**, 66 (2010).

[8] K. Langanke and H. Schatz, Physica Scripta **2013**, 014011 (2013).

[9] K. Smith, A. M. Amthor, R. Cyburt, R. Ferguson, A. Heger, E. Johnson, M. Klein, Z. Meisel, T. Rauscher, A. Sakharuk, et al., Bulletin of the American Physical Society **53** (2008).

[10] S. Gupta, E. F. Brown, H. Schatz, P. Möller, and K.-L. Kratz, The Astrophysical Journal **662**, 1188 (2007).

[11] Haensel P and Zdunik J L 2003 Astron. Astrophys. **404,** L33 (2003).

[12] C. E. Rolfs and W. S. Rodney, *Cauldrons in the cosmos: Nuclear astrophysics* (University of Chicago press, 1988).

[13] L. Zhi-Hong, Chinese Physics Letters **23**, 3219 (2006).

[14] J. José and M. Hernanz, The Astrophysical Journal **494**, 680 (1998).

[15] S. Bishop, R. Azuma, L. Buchmann, A. Chen, M. Chatterjee, J. DAuria, S. Engel, D. Gigliotti, U. Greife, M. Hernanz, et al., Physical review letters **90**, 162501 (2003).

[16] L. N. Downen, C. Iliadis, J. José, and S. Starrfield, The Astrophysical Journal **762**, 105 (2012).

[17] H. Schatz, A. Aprahamian, V. Barnard, L. Bildsten, A. Cumming, M. Ouellette, T. Rauscher, F.-K. Thielemann, and M. Wiescher, Physical Review Letters **86**, 3471 (2001).

[18] M. Zamfir, A. Cumming, and D. K. Galloway, The Astrophysical Journal **749**, 69 (2012).

[19] C. Tur, A. Heger, and S. M. Austin, The Astrophysical Journal **718**, 357 (2010).

[20] L. F. Roberts, W. R. Hix, M. Smith, and J. L. Fisker, in *International Symposium on Nuclear Astrophysics-Nuclei in the Cosmos-IX* (2006), vol. 25, p. 30.

[21] M. Wiescher, in *Journal of Physics: Conference Series* (IOP Publishing, 2013), vol. 420, p. 012135.

[22] K. Chipps, D. Bardayan, C. Nesaraja, S. Pain, M. Smith, J. Blackmon, K. Chae, B. Moazen, S. Pittman, U. Greife, et al., in *Nuclei in the Cosmos (NIC X)* (2008).

[23] M. Couder, private communication.

[24] G. Berg, D. Bardayan, J. Blackmon, K. Chipps, M. Couder, U. Greife, U. Hager, F. Montes, K. Rehm, H. Schatz, et al., Nuclear Instruments and Methods in Physics Research Section B: Beam Interactions with Materials and Atoms **376**, 165 (2016).

[25] D. Shapira, T. Lewis, and L. Hulett, Nuclear Instruments and Methods in Physics Research Section A: Accelerators, Spectrometers, Detectors and Associated Equipment **454**, 409 (2000).

[26] K. Birkinshaw, Journal of mass spectrometry **32**, 795 (1997).

[27] W. R. Leo, *Techniques for nuclear and particle physics experiments: a how-to approach* (Springer Science & Business Media, 2012).

[28] A. James, P. Butler, T. Morrison, J. Simpson, and K. Connell, Nuclear Instruments and Methods in Physics Research **212**, 545 (1983).

[29] K. Chipps, D. W. Bardayan, C. Nesaraja, M. Smith, J. Blackmon, K. Chae, B. Moazen, S. Pittman, U. Greife, R. Hatarik, et al., Physical Review C **80**, 065810 (2009).

[30] J. Lai, Louisiana State University Ph.D. Thesis. (2016).

[31] A. Al-Adili, F.-J. Hambsch, R. Bencardino, S. Pomp, S. Oberstedt, and S. Zeynalov, Nuclear Instruments and Methods in Physics Research Section A: Accelerators, Spectrometers, Detectors and Associated Equipment **671**, 103 (2012).

[32] J. Thomas, D. Bardayan, J. Blackmon, J. Cizewski, U. Greife, C. Gross, M. Johnson, K. Jones, R. Kozub, J. Liang, et al., Physical Review C **71**, 021302 (2005).

[33] C. Wrede, in *EPJ Web of Conferences* (EDP Sciences, 2015), vol. 93, p. 07001.

VITA

Kyle Joerres was born in Wisconsin. He got his Bachelor of Science from St. Norbert college in 2015. Afterwards he made the decision to enter graduate school in the Department of Physics and Astronomy at Louisiana State University. He hopes to receive his Master's degree in 2017.